

[illegible]

2



570
MAR 08 1962

X. K. Maruyama

Approved for public release; distribution is unlimited

92-05256



002

REPORT DOCUMENTATION PAGE

Form Approved
OMB No. 0704-0188

1 REPORT SECURITY CLASSIFICATION Unclassified		1b RESTRICTIVE MARKINGS	
2 SECURITY CLASSIFICATION AUTHORITY		3 DISTRIBUTION AVAILABILITY OF REPORT Approved for public release; distribution is unlimited.	
5 DECLASSIFICATION/DOWNGRADING SCHEDULE		5 MONITORING ORGANIZATION REPORT NUMBER(S)	
PERFORMING ORGANIZATION REPORT NUMBER(S)			
6a NAME OF PERFORMING ORGANIZATION Naval Postgraduate School	6b OFFICE SYMBOL (If applicable) 33	7a NAME OF MONITORING ORGANIZATION Naval Postgraduate School	
c ADDRESS (City, State, and ZIP Code) Monterey, CA 93943-5000		7b ADDRESS (City, State, and ZIP Code) Monterey, CA 93943-5000	
8a NAME OF FUNDING SPONSORING ORGANIZATION	8b OFFICE SYMBOL (If applicable)	9 PROCUREMENT INSTRUMENT IDENTIFICATION NUMBER	
3c ADDRESS (City, State, and ZIP Code)		10 SOURCE OF FUNDING NUMBERS	
		PROGRAM ELEMENT NO	PROJECT NO
		TASK NO	WORK UNIT ACCESSION NO
11 TITLE (Include Security Classification) EFFECTS OF HIGH ENERGY ELECTRON IRRADIATION ON A $\text{YBa}_2\text{Cu}_3\text{O}_{7-\delta}$ HIGH TEMPERATURE SUPER-CONDUCTOR			
12 PERSONAL AUTHOR(S) Connors, Sean Mark			
13a TYPE OF REPORT Master's Thesis	13b TIME COVERED FROM _____ TO _____	14 DATE OF REPORT (Year, Month, Day) 1991, September	15 PAGE COUNT 104
16 SUPPLEMENTARY NOTES The views expressed in this thesis are those of the author and do not reflect the official policy or position of the Department of Defense or the U.S. Government.			
17 COSATI CODES		18 SUBJECT TERMS (Continue on reverse if necessary and identify by block number)	
FIELD	GROUP	SUB-GROUP	
		HIGH TEMPERATURE SUPERCONDUCTORS, IRRADIATION EFFECTS, ELECTRON IRRADIATION, SUPERCONDUCTIVITY, DOSIMETRY	
19 ABSTRACT (Continue on reverse if necessary and identify by block number) High quality, single crystalline, high-temperature superconductors ($\text{YBa}_2\text{Cu}_3\text{O}_{7-\delta}$) were irradiated with 88.5 and 92.0 MeV electrons at various fluences to a maximum of $2.5 \pm 0.5 \times 10^{18}$ electrons/cm ² . The samples were manufactured at the Texas Center for Superconductivity at the University of Houston and this experiment was in support of a much larger experiment investigating the effects of various irradiations on the critical current. By introducing artificial pinning centers, such as those produced by electron irradiation, in high-temperature superconductors, an applied magnetic flux can be effectively pinned and the current carrying capacity can be increased. By comparing the critical current density enhancement effects to the total atomic displacement damage, it is found that the enhancement depends heavily on the type and energy of radiation and on the beam direction with respect to the crystal. It was also found that a threshold defect-size for effective flux pinning exists. Cascade defects, 10-20 Å and larger, are at least a thousand times more effective than point defects as			
20 DISTRIBUTION AVAILABILITY OF ABSTRACT <input checked="" type="checkbox"/> UNCLASSIFIED, LIMITED <input type="checkbox"/> SAME AS RPT <input type="checkbox"/> DTIC USERS		21 ABSTRACT SECURITY CLASSIFICATION Unclassified	
22a NAME OF RESPONDER (Individual) Professor Xavier K. Maruyama		22b TELEPHONE (Include Area Code) (408) 646-2431	22c OFFICE SYMBOL PH/MX

Block 19. Abstract (Continued)

pinning centers. A critical measurement required for this experiment is the determination of the dose and the electron beam profile incident on the $\text{YBa}_2\text{Cu}_3\text{O}_7$ samples. Methods of monitoring the beam for both real-time and post experimental analysis were developed so that the dose and fluence could easily be determined. Additionally, methods by which the products of the irradiation were identified and their respective activities calculated are also presented. This work may serve as a reference for similar, future experiments requiring a thorough and complete understanding of electron irradiation.

Approved for public release; distribution is unlimited.

EFFECTS OF HIGH ENERGY ELECTRON IRRADIATION ON A
 $\text{YBa}_2\text{Cu}_3\text{O}_{7-\delta}$ HIGH TEMPERATURE SUPERCONDUCTOR

by

Sean M. Connors
Lieutenant, United States Navy
B.S., United States Naval Academy, 1986

Submitted in partial fulfillment
of the requirements for the degree of

MASTER OF SCIENCE IN PHYSICS

from the

NAVAL POSTGRADUATE SCHOOL

September 1991

Author:

Sean M. Connors

Sean M. Connors

Approved by:

Xavier K. Maruyama

Xavier K. Maruyama, Thesis Advisor

F. R. Buskirk

F. R. Buskirk, Second Reader

Karlheinz E. Woehler

Karlheinz E. Woehler, Chairman,
Department of Physics

Accession For

NAME

DATE

BY

NO.

CLASS

STATUS

REMARKS

DATE

BY

NO.

CLASS

STATUS

REMARKS

DATE

BY

NO.

CLASS

STATUS

REMARKS

DATE

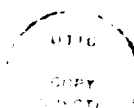
BY

NO.

CLASS

STATUS

REMARKS



A-1

ABSTRACT

High quality, single crystalline, high-temperature superconductors ($\text{YBa}_2\text{Cu}_3\text{O}_{7-\delta}$) were irradiated with 88.5 and 92.0 MeV electrons at various fluences to a maximum of $2.5 \pm 0.5 \times 10^{18}$ electrons/cm². The samples were manufactured at the Texas Center for Superconductivity at the University of Houston and this experiment was in support of a much larger experiment investigating the effects of various irradiations on the critical current. By introducing artificial pinning centers, such as those produced by electron irradiation, in high-temperature superconductors, an applied magnetic flux can be effectively pinned and the current carrying capacity can be increased. By comparing the critical current density enhancement effects to the total atomic displacement damage, it is found that the enhancement depends heavily on the type and energy of radiation and on the beam direction with respect to the crystal. It was also found that a threshold defect-size for effective flux pinning exists. Cascade defects, 10-20 Å and larger, are at least a thousand times more effective than point defects as pinning centers. A critical measurement required for this experiment is the determination of the dose and the electron beam profile incident on the $\text{YBa}_2\text{Cu}_3\text{O}_{7-\delta}$ samples. Methods of monitoring the beam for both real-time and post experimental analysis were developed so that the dose and fluence could easily be determined. Additionally, methods by which the products of the irradiation were identified

and their respective activities calculated are also presented. This work may serve as a reference for similar, future experiments requiring a thorough and complete understanding of electron irradiation.

TABLE OF CONTENTS

I. INTRODUCTION	1
A. PURPOSE OF EXPERIMENT	1
B. PREVIOUS WORK	2
1. High Energy Election Irradiation	2
2. Dosimetry	4
C. OVERVIEW OF EXPERIMENT	5
II. ELECTRON BEAM DIAGNOSIS	7
A. DOSIMETRY	7
1. Calculated Dose	7
2. Measured Dose	13
B. FLUENCE	17
III. EXPERIMENTAL SETUP, PROCEDURES AND ANALYSIS	29
A. EQUIPMENT SETUP	29
B. PROCEDURE	34
1. Alignment	34
2. Irradation	36
C. ANALYSIS	37
1. Identification	37
2. Activity	45

IV. EXPERIMENTAL RESULTS	46
A. RESULTS	46
B. CONCLUSIONS	51
C. RECOMMENDATIONS	53
APPENDIX A: LINAC CHARACTERISTICS	A-1
APPENDIX B: SEM CALIBRATION	B-1
APPENDIX C: SUPERCONDUCTIVITY THEORY	C-1
APPENDIX D: SUBMISSION OF RESULTS TO APL, June 7,1991: "Defect Size Dependence of Critical Current Density Enhancement For Irradiated YBa ₂ Cu ₃ O _{7-δ} "	D-1
LIST OF REFERENCES	54
BIBLIOGRAPHY	56
INITIAL DISTRIBUTION LIST	57

ACKNOWLEDGEMENTS

I wish to thank Xavier Maruyama for providing me with the opportunity to explore this new field as a thesis. His enduring patience, guidance and optimism made the entire process both instructive and fun.

Thanks also to Jeff Bechtold of the University of Houston who supplied the original idea for this continued research into High Temperature Superconductors, and whom also gave me an unlimited amount of guidance in my thesis preparation.

A special thanks to Don Snyder and Harold Rietdyk, for without them life at the LINAC would not be the same and frankly I doubt whether it would exist at all.

Finally, but foremost, I wish to thank my wife, Mikala, for her never ending patience and support while caring for me and our daughter, Kilii. It wasn't easy taking care of us "kids." I dedicate this work to her.

I. INTRODUCTION

A. PURPOSE OF EXPERIMENT

Since the discovery of high temperature superconductors (HTSs) the scientific community has continually been attempting to exploit the potential applications of their extraordinary electromagnetic properties. One obstacle which must be overcome however, is the relatively low current densities measured in bulk superconducting samples. Towards this goal, it is theorized that by introducing artificial pinning centers in HTSs, such as with electron irradiation, an applied magnetic flux can be effectively pinned, thereby increasing its current carrying capacity. This change in critical current (J_c) is thought to be dependent upon the size of the pinning site, which, in turn, is heavily dependent on the type and energy of irradiation. As part of a much larger experiment examining the effects of different irradiations at various energies on J_c , high energy electron irradiation was performed at the linear accelerator (LINAC) at the Naval Postgraduate School.

To determine the effects of electron irradiation on the critical current in Y-Ba₂Cu₃O_{7.8} (Y123), it is necessary to know how much radiation was incident on each of the samples. A critical measurement therefore is the determination of dose and the electron beam profile incident on each sample. The purpose of this experiment, therefore, was to develop a method to monitor the electron beam, so

that both real-time and post experimental analysis could be performed and the fluence and dose easily calculated. Furthermore, to gain a full understanding of the electron-Y123 interaction, methods were determined to identify the products of the irradiation and to calculate their respective activities. These procedures can be extended to any similar experiment at the linear accelerator (LINAC) so that electron irradiation can be more thoroughly understood.

B. PREVIOUS WORK

1. High Energy Electron Irradiation

Recent work at the Naval Postgraduate School LINAC has concentrated on the electron radiation effects on resistance and critical temperature of Y123 as well as its "resistance" to radiation. Sweigard [Ref. 1] observed a slight increase in the normal state resistance and a small decrease in critical temperatures after irradiation to high doses (greater than 1 megarad). Wolfe [Ref. 2] observed a similar change in the normal state resistance and a slight shift in the transition temperature after high doses and also concluded that the Y123 superconductor is sufficiently "hard" for high radiation environments. Wolfe's experiment showed that the effects were similar whether the irradiation was done at liquid nitrogen temperatures or at room temperatures. Hammerer [Ref. 3] observed neutron irradiation effects in reactor irradiated samples and observed a complete loss of

superconductivity in Y123 at fluences on the order of 10^{18} fast and thermal neutrons/cm².

Elsewhere, investigation of HTS properties has exploded since the discovery of high temperature superconductors by C.W. Chu at the University of Houston. It has been shown by the University of Houston that low energy electron and gamma irradiation have little effect on the critical current. Likewise, ion bombardment has proved futile in enhancing the critical current [Ref. 4]. Several experiments, using fast neutron irradiation, have shown an increased critical current in bulk crystalline samples of Y123 by factors of 10 to 100 [Refs. 5,6,7]. Likewise, 3 MeV electrons were found to also enhance J_c on the same order of magnitude as neutron bombardment, but a marked decrease in J_c was discovered upon further irradiation. This suggests a threshold for the enhancement [Refs. 8,9,10].

Other research with HTS's has studied the quality of samples to explain irradiation effects. Nastasi et al. [Ref. 11] observed that the electron dose required to initiate interstitials and hence pinning sites is lower for grain boundary irradiations as compared to large single grain irradiations. To examine this further, Vichery et al. [Ref. 12] conclusively showed that degradations in the critical temperature and the normal state resistivity resulted from intragrain damage in single crystalline samples. While examining the crystal structure of Y123, Rullier-Albenque et al. [Ref. 13] and Meyer [Ref. 4] found a drastic decrease

in T_c when the concentration of oxygen vacancies increased and concluded that the superconducting properties are not only determined by the composition and the defect structure but also by the amount and lattice location of the oxygen. Follow on experiments by Vichery et al. [Ref. 12] and Hoffmann et al. [Ref. 14] suggest that it is more likely to assume that displaced copper atoms also affect the transport properties in irradiated Y123. Nevertheless, it appears that the initial state of the sample probably affects the irradiation response. Although there has been much research and many conclusions drawn in very specific areas, it is clear that a more complete and systematic research is necessary to fully understand the effects of particle irradiation on the critical current.

2. Dosimetry

Dosimetry is a key component of the experiment to determine the effects of radiation on the critical current. Previous work done at the LINAC in calculating the dose on radiated samples was done by one of two different methods. Sweigard [Ref. 1] performed a lengthy and complicated calculation which yields a calculated dose; whereas, Wolfe [Ref. 2] used a thermoluminescent dosimeter (TLD) to measure the dose. Although the latter method will yield a dose very quickly to a known charge accumulation, the dose given will be for a TLD chip and therefore only an approximation of the dose on an irradiated target.

C. OVERVIEW OF EXPERIMENT

In this experiment several high quality, single crystal Y123 samples were exposed to various doses and at different angles relative to the crystalline c-axis. A more thorough discussion of the crystal structure and an overview of Superconductor theory is contained in Appendix C. To examine the effects of irradiation on $J_c T_c$ and the resistivity, ρ , two runs were conducted using 88.5 MeV and 92.0 MeV electron beams produced by the linear accelerator (LINAC), located at the Naval Postgraduate School (NPS), Monterey, California.

The samples were manufactured by the Texas Center for Superconductivity at the University of Houston (TCSUH). High quality (single crystal) samples were used because sample inhomogeneities are sensitive to radiation damage and result in the growth of an amorphous phase within the sample. It was felt that the lack of quality in previous samples is the main reason for the inconsistencies of earlier irradiation experiments. Therefore, single crystal, high quality samples were used. The samples were exposed to various doses and the resistance and temperature, as well as the critical current were measured both prior to and after irradiation.

To determine the fluence and dose on each Y123 sample, optical transition radiation (OTR) images were used to profile the electron beam during the experiment. A secondary emission monitor (SEM) was used to monitor the electron beam's current. From these measurements, the dose was calculated and then compared to a measured dose obtained from TLD dosimetry. Technical

problems with the LINAC precluded TLD dosimetry from being accomplished during the first run and, therefore, was performed on the second run only.

After irradiation, a NaI(Tl) detector was used for pulse height analysis to identify and measure activation induced in the superconducting samples during irradiation.

This paper will serve as a reference for conducting the different aspects of an irradiation experiment at the NPS LINAC such as monitoring the beam, calculating fluence and dose, identifying the radioactive isotopes of the irradiation and calculating their respective activities.

II. ELECTRON BEAM DIAGNOSTICS

A. DOSIMETRY

1. Calculated Dose

When high energy electrons, as from an electron beam, bombard a target several things may happen. The electron may pass through undeflected or it may be deflected and absorbed, each time losing energy. The energy lost per unit path length is called the specific energy loss, and the energy losses due to ionization and excitation, or collisional losses may be calculated by:

$$-\left(\frac{dE}{dx}\right)_c = \frac{2\pi e^4 N Z}{m_0 V^2} \left[\ln \frac{m_0 V^2 E}{2 I (1 - \beta^2)} - \ln 2 (2\sqrt{1 - \beta^2} - 1 + \beta^2) + (1 - \beta^2) + \frac{1}{8} (1 - \sqrt{1 - \beta^2})^2 \right] \quad (1)$$

Where e = electron charge, N = number density of absorber atoms, Z = atomic number of absorber atoms, m_0 = electron rest mass, v = electron velocity, E = electron energy in MeV, I = average ionization and excitation potential of the absorber and β = relativistic velocity ratio (v/c) [Ref. 15]. This expression describes the specific energy losses of low energy electrons and is nearly the same as that from protons [Ref. 15]. Equation (1) is difficult to calculate reliably because I must be obtained empirically and may not be readily available. Unlike the more massive proton, when electrons are accelerated to high energies and their velocities become relativistic; the electrons are more apt to scatter several times, each time

changing its velocity in both magnitude and direction. These accelerations cause the electrons to radiate bremsstrahlung radiation and the associated radiative specific energy loss is given by [Ref. 15]:

$$-\left(\frac{dE}{dx}\right)_{rad} = \frac{NEZ(Z+1)e^4}{137(M_0C^2)^2} \left(4 \ln \frac{2E}{M_0C^2} - \frac{4}{3}\right) \quad (2)$$

By inspection, radiative energy loss is more significant for high energy electrons and for absorber atoms of high atomic numbers. The total energy loss of the electrons as they pass through a target is called the total linear stopping power and is given by the sum of the collisional and radiative specific energy losses:

$$\frac{dE}{dx} = \left(\frac{dE}{dx}\right)_c + \left(\frac{dE}{dx}\right)_{rad} \quad (3)$$

The two expressions (1) and (2) give a convenient numerical approximate ratio:

$$\frac{\left(\frac{dE}{dx}\right)_{rad}}{\left(\frac{dE}{dx}\right)_c} = \frac{EZ}{700} \quad (4)$$

With E in MeV.

Using these relationships one can determine the percentages of energy lost due to radiation and collision. First calculate the ratio, $EZ/700$ and $(dE/dx)_{rad}$ for

each absorber atom. Then from equation (4), $(dE/dx)_c$ may be determined. The percentage of energy lost due to either radiation or collisions for each absorber atom may then be found. Table I shows the contributions of radiative and collisional energy losses due to each absorber atom for both runs of the experiment. Note that there is very little difference between the results of the two runs since the energies were almost the same.

TABLE I
ENERGY LOSS DISTRIBUTION DUE TO RADIATION AND IONIZATION

ABSORBER ATOM	ATOMIC NUMBER Z	NUMBER DENSITY N	RUN 1: E=88.5 MeV		RUN 2: E=92.0 MeV	
			$\%(dE/dX)_{rad}$	$\%(dE/dX)_c$	$\%(dE/dX)_{rad}$	$\%(dE/dX)_c$
Y	39	1	83.1	16.9	83.2	16.8
Ba	56	2	87.6	12.4	87.6	12.4
Cu	29	3	78.6	21.4	78.6	21.4
O	8	7	50.2	49.8	50.2	49.8

To calculate the percentage of energy lost due to either radiation or collisions for each run, simply sum the products of each absorber atoms percentage of specific energy loss ($\%(dE/dx)$) with the associated number density, N, and divide by the sum of all number densities. For example; the percentage

of energy lost due to radiation for Y123 in the first run may be found by the following operation:

$$\bar{x}(\text{rad}) = [(83.1)(1) + (87.6)(2) + (78.6)(3) + (50.2)(7)]/13 \quad (5)$$

This calculation yielded the same approximation for both runs:

Y123 = 65.0% of energy lost due to radiation

Y123 = 35.0% of energy lost due to collisions/ionization

For radiation effect studies, in general, radiative losses may be neglected because the average sample thickness for each run was approximately 0.5 mm and most of the bremsstrahlung radiation would have escaped the samples without further significant energy exchanges [Ref. 1].

After neglecting radiative losses, to determine the specific energy losses for the Y123 compound it is first necessary to find the specific energy losses for the compounds' constituents. These may be found by interpolation of experimentally determined specific energy loss values for atoms as tabulated in Reference 16. As oxygen and copper are the only elements of the Y123 compound listed in Reference 16; it is first necessary to establish a relationship so that a conversion factor can be applied to those elements listed to determine the values of the remaining constituents of the compound.

By inspection of Equation 1, the collisional specific energy loss of each absorber atom is proportional to the product of the number density with the atomic number. Therefore the following relationship must also be true:

$$\left(\frac{dE}{dx}\right)_c \propto \frac{Z}{A} \quad (6)$$

where Z is the atomic number of the absorber atom and A is its associated atomic weight. Due to this relationship, tabulated specific energy losses of elements nearest in atomic number to those constituents not listed can be used to calculate the specific energy loss for each of the Y123 absorber atoms. Therefore the following expression may be established for calculating $(dE/dx)_c$ for the constituents in question:

$$\left(\frac{dE}{dx}\right)_2 = \frac{\left(\frac{Z}{A}\right)_2}{\left(\frac{Z}{A}\right)_1} \left(\frac{dE}{dx}\right)_1 \quad (7)$$

where subscript 1 implies the known interpolated values and subscript 2 implies the specific constituent of the Y123 compound. A weighted value for each constituent may then be calculated by multiplying the specific energy loss with the number density of the absorber atom and then dividing by the sum of all the number densities for the compound.

Tables II and III summarize the foregoing procedure for the Y123 compound for runs 1 and 2 respectively. Also included in Table II are the tabulated values for CaF_2 , a TLD used for dosimetry in the second run. In Table II, note that two elements, Oxygen and Neon, were used for Fluorine due to the proximity of their atomic numbers and the weighted value listed is the average of the two.

TABLE II
COLLISIONAL SPECIFIC ENERGY LOSS VALUES, RUN 1

Run 1: E=88.5 MeV							$(\frac{dE}{dx})_1$	$(\frac{dE}{dx})_2$	Weighted
At	N ₂	Z ₂	A ₂	Atom ₁	Z ₁	A ₁	$[\frac{\text{MeV}}{\text{gm/cm}^2}]$	$[\frac{\text{MeV}}{\text{gm/cm}^2}]$	$(\frac{dE}{dx})_2$ $[\frac{\text{MeV}}{\text{gm/cm}^2}]$
Y	1	39	88.91	Kr	36	83.80	1.920	1.961	0.151
Ba	2	56	137.33	Xe	54	131.30	1.786	1.771	0.272
Cu	3	29	63.55	Cu	29	63.55	1.660	1.660	0.383
O	7	8	16.00	O	8	16.00	2.407	2.407	1.296

TABLE III
COLLISIONAL SPECIFIC ENERGY LOSS VALUES, RUN 2

Run 2: 92 MeV							$(\frac{dE}{dx})_1$	$(\frac{dE}{dx})_2$	Weighted
Atom ₂	N ₂	Z ₂	A ₂	Atom	Z ₁	A ₁	$[\frac{\text{MeV}}{\text{gm/cm}^2}]$	$[\frac{\text{MeV}}{\text{gm/cm}^2}]$	$(\frac{dE}{dx})_2$ $[\frac{\text{MeV}}{\text{gm/cm}^2}]$
Y	1	39	88.91	Kr	36	83.80	1.926	1.967	0.151
Ba	2	56	137.33	Xe	54	131.30	1.793	1.778	0.274
Cu	3	29	63.55	Cu	29	63.55	1.663	1.663	0.384
O	7	8	16.00	O	8	16.00	2.413	2.413	1.299
Ca	1	20	40.08	Ar	18	39.95	2.099	2.324	0.775
F	2	9	19.00	O	8	16.00	2.413	2.286	1.523
				Ne	10	20.18	2.386	2.281	

Summing the weighted values for Y123 and CaF yields the following specific energy losses for both runs:

$$\left(\frac{dE}{dx}\right)_{Y123} = 2.102 \text{ MeV/gm/cm}^2 \quad [\text{Run 1}] \quad (8)$$

$$\left(\frac{dE}{dx}\right)_{Y123} = 2.108 \text{ MeV/gm/cm}^2 \quad [\text{Run 2}] \quad (9)$$

$$\left(\frac{dE}{dx}\right)_{CaF_2} = 2.298 \text{ MeV/gm/cm}^2 \quad [\text{Run 3}] \quad (10)$$

Multiplying the specific energy loss for the Y123 compound by the fluence (electrons/cm²) of each sample and the conversions of 1.6×10^{-6} ergs/MeV and 1 Rad/100 ergs/gm will yield the calculated dose on the Y123 samples for each run. The only unknown variable left is the fluence, which will be discussed in a later section. The specific energy losses for both Y123 and CaF₂ will be used in a correction to the measured dose so that it may be compared to the calculated value.

2. Measured Dose

Measuring the dose from the electron beam was accomplished using calcium-fluoride (CaF₂) thermoluminescent dosimeters (TLD's) and then multiplying the value obtained by a correction factor to yield the dose for a Y123 sample. CaF₂ TLDs were used due to their linear response over a large range of absorbed dose. The CaF₂ chips were placed in the corner of a plastic bag at the front and center of the target chamber. When the electrons in the beam strike the

TLD, the electrons in the TLD are elevated from the conduction band to the valence band and become trapped. After an exposure, the TLD's are heated slowly in a TLD reader and when the temperature is high enough for the trapped electrons to obtain the required energy to re-excite back to the conduction band, a radiated photon in the visible region results. Through the use of a photomultiplier tube, the total number of photons are related to the radiation exposure, and hence dose. Although the saturation level for the TLD reader is approximately 7-8 kilorads, high doses can be determined by establishing a dose to integrated electron current ratio [Ref. 1].

To determine the integrated electron beam current passing through the TLD chip to be used for the charge-dose conversion plot, a Secondary Emissions Monitor (SEM) was used. For this experiment the SEM was placed in the path of the electron beam downstream of the target. The SEM uses extremely thin aluminum foils which emit secondary electrons when hit by the incident beam. These secondary electrons are used to charge a capacitor and create a voltage across it. This voltage is then a measure of the integrated charge collected across the capacitor and is given by:

$$Q_{SEM} = CV \tag{11}$$

where Q_{SEM} is the charge on the capacitor within the SEM, C is the known capacitance and V is the integrated voltage. From this relationship a voltage-dose conversion plot is obtained.

The number of electrons which pass through the SEM can be determined from:

$$N_{SEM} = \frac{CV}{e} \quad (12)$$

where N_{SEM} is the number of electrons through the SEM, and e is the electronic charge per electron.

A calibration was performed on the SEM against a Faraday cup at the beginning of the experiment and it was determined that the efficiency of the SEM is 12.7 +/- 0.5 percent. This calibration is discussed in Appendix B. Therefore, the total number of electrons passing throughout the target, N , is:

$$N = \frac{N_{SEM}}{0.127} \quad (13)$$

This relationship was used to calculate the fluence.

Through a voltage-dose conversion plot, the dose on a CaF_2 TLD at the front and in the center of the target chamber has been measured. To convert this dose to the dose on a Y123 sample located throughout the target chamber, a

correction factor must be applied. All the Y123 samples in the chamber for run 2 were centrally located and were well within the full width at half maximum (FWHM) of the electron beam; therefore, only the sample displacement from the front edge of the target and the difference in the compounds composition must be taken into account.

To account for the different composition, recall that the calculated dose was proportional to the total collisional specific energy loss. It follows then that the dose on a Y123 sample is proportional to the dose and a CaF_2 TLD by the relationship:

$$DOSE_{Y123} = \frac{\left(\frac{dE}{dx}\right)_{Y123}}{\left(\frac{dE}{dx}\right)_{\text{CaF}_2}} \times DOSE_{\text{CaF}_2} \quad (14)$$

To further account for the displacement from the front edge of the target chamber, recall also that the calculated dose is proportional to the fluence and inversely proportional to the area. Therefore, the following relationship holds:

$$DOSE_2 = \frac{A_1}{A_2} \times DOSE_1 \quad (15)$$

where A represents the electron beam area and subscripts 1 and 2 represent the front edge of the target chamber and the point in question in the target chamber respectively. Combining these corrections, the measured dose is then given by the relation:

$$DOSE_{MEAS} = \frac{(\frac{dE}{dx})_{Y123}}{(\frac{dE}{dx})_{CaF_2}} \times (\frac{D_1}{D_2})^2 \times DOSE_{CaF_2} \quad (16)$$

where the specific energy losses are those calculated in the previous section, D refers to the electron beam diameter (its method of determination will be discussed in the next section), Dose CaF₂ is the dose obtained from the voltage-dose conversion plot and subscripts 1 and 2 denote the front edge of the target chamber and the point in question in the target chamber respectively, as before.

Figure 1 is the voltage-dose conversion plot for run 2 of the experiment. The calculated dose for the first run and a comparison of both dose determination methods for the second run is contained in the Results section.

B. FLUENCE

Fluence is defined as the number of electrons crossing a unit area and may be expressed as:

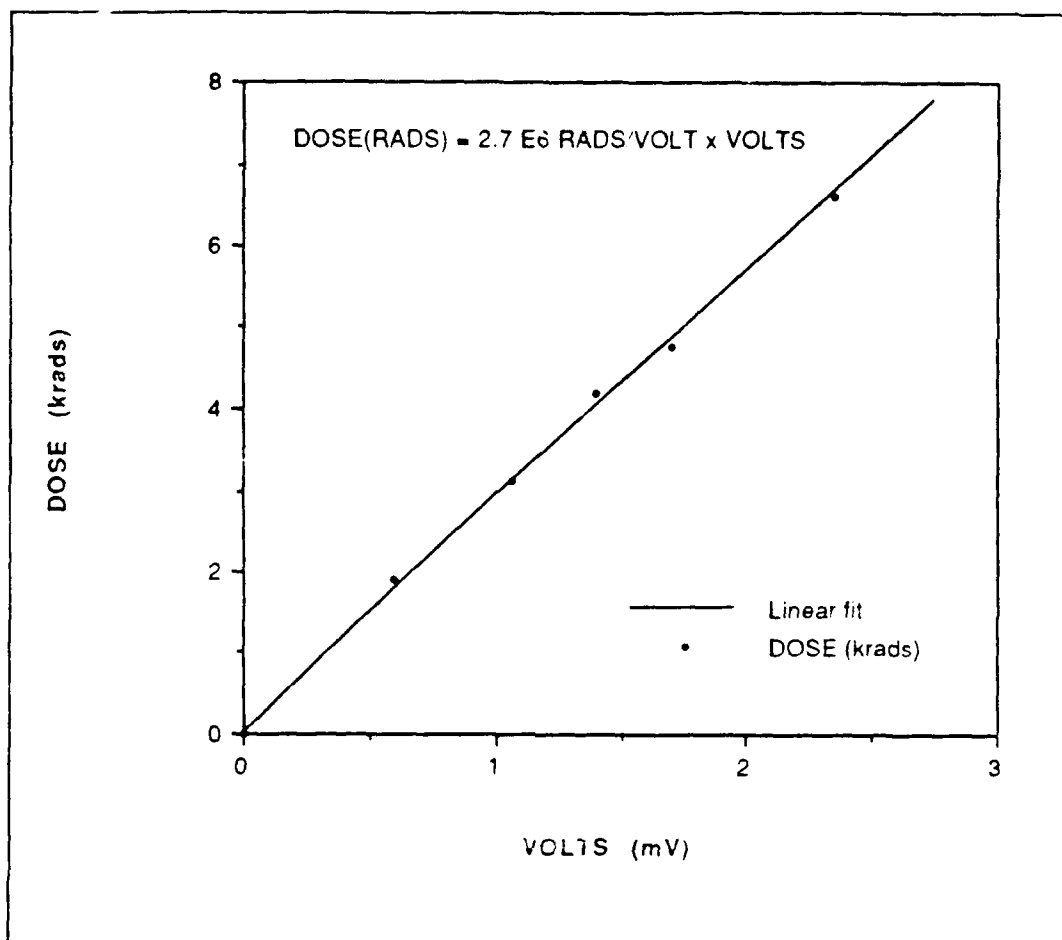


Figure 1. Dose vs. SEM Voltage

$$\phi = N/A$$

(17)

where ϕ represents the fluence, N is the number of electrons and A is the electron beam area. The number of electrons can be calculated as described earlier, and it is only a matter of determining the electron beam's area to calculate the fluence.

To determine the electron beam area in this experiment, two techniques were

used to obtain the electron beam profile entering and exiting the target chamber which contained all the Y123 samples. The first was optical transition radiation (OTR). Transition radiation is that radiation emitted from a charged particle as it crosses a boundary between two media with different dielectric constants. It appears as broad band radiation and is used for detection of high energy charged particles and as a diagnostic tool for low energy and relativistic beams [Ref. 17]. Furthermore its spectrum may extend from the microwave to x-ray frequencies and the polarized photons produced are generated in both the forward and backward directions. It has been shown that the visible portion of transition radiation (OTR) can be used since cameras and other optical equipment are readily available for observation at these wavelengths [Ref. 17]. The second method used to profile the electron beam was done by applying a thin layer of phosphor on a surface which the beam penetrates. When the electrons strike the phosphor, visible photons are observed.

During the experiment, cameras connected to video monitors and a frame grabber board in a MacIntosh computer allowed us to monitor the electron beam on line and also to store the images for post experimental analysis. From these displays, it is shown that the electron beam both entering and leaving the target chamber was approximately Gaussian in shape (see Figures 2 through 5). Figure 2 is the OTR from the front of the target chamber, Figure 3 is the beam intensity

from phosphorescence off the back of the target chamber and Figures 4 and 5 are representative cuts from these profiles used to determine the beam size.

From the target chamber arrangement, the locations of each plate and mounted samples were known. If the electron beam size was known going in and coming out of the chamber one could assume that the electron beam scattered at each plate interface and therefore the increases throughout the target chamber would be discrete. The electron beam diameter would then increase by an average "step" at each plate, where each step would be the difference between the beam size entering and leaving the target chamber divided by the number of sample plates contained in the chamber. Because the beam varied over time and was turned off and on to change samples several times, the exact beam parameters were not known at all times. To better understand the beam area, one must understand the charge distribution throughout the target chamber.

The three-dimensional electron beam profile may be represented by a Gaussian function given by:

$$\rho(r) = \rho_0 e^{\frac{-r^2}{2\sigma^2}} \quad (18)$$

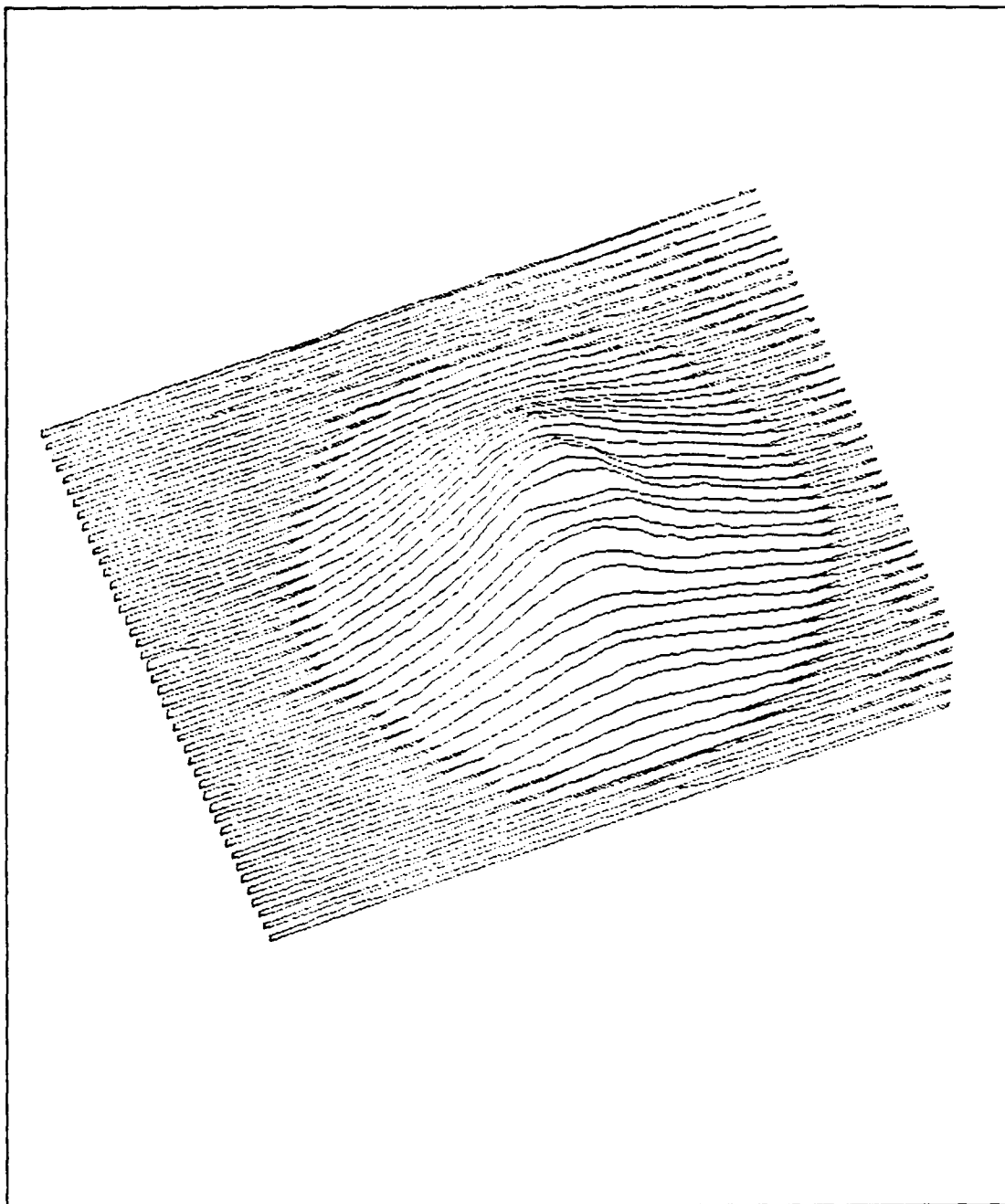


Figure 2. Beam Intensity Profile as Measured by
OTR from Front Surface of Target Chamber

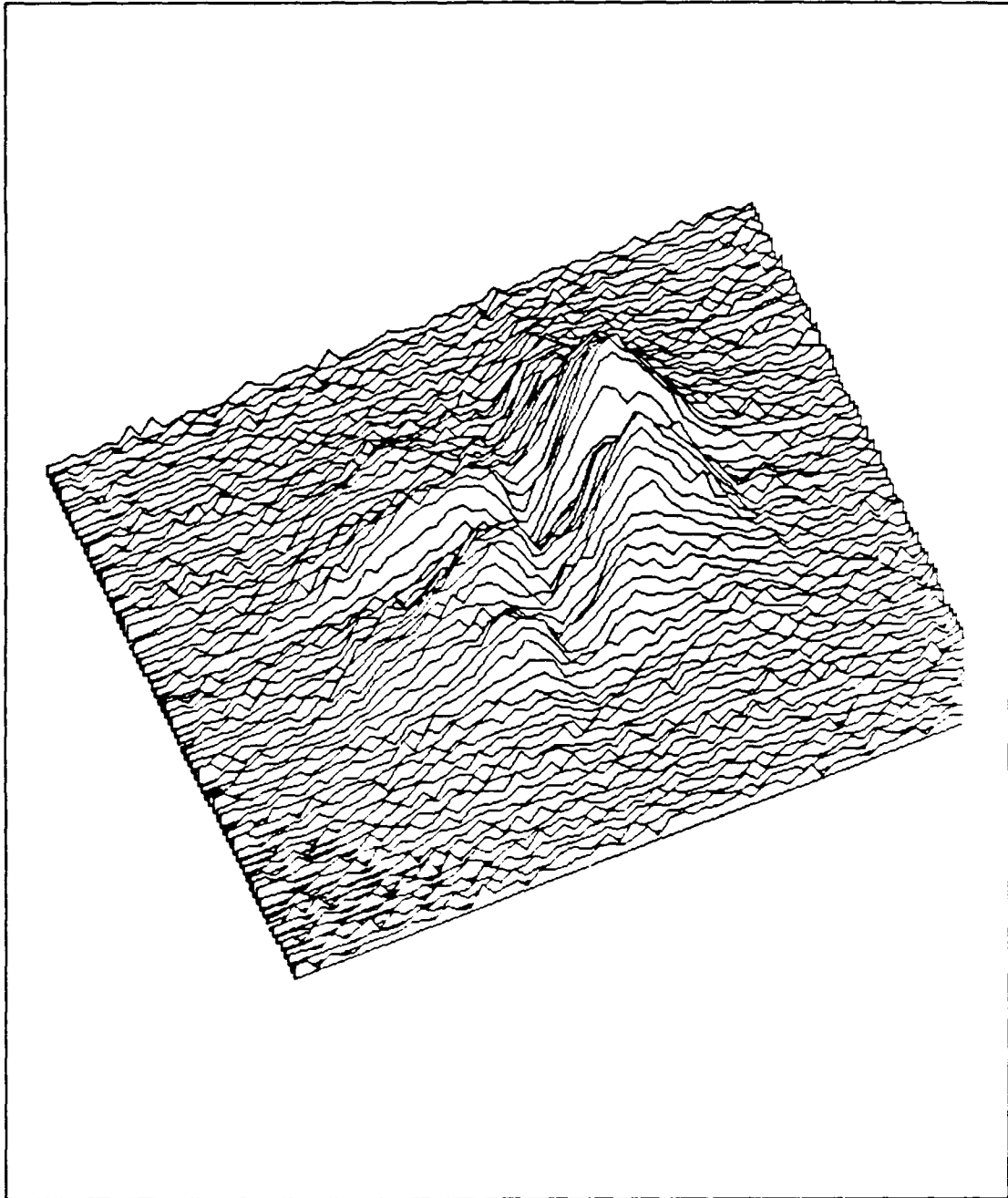


Figure 3. Beam Intensity Profile as Measured with Phosphor from the Back Surface of the Target Chamber. The perpendicular indentations in the profile are due to cross hair pencil marks on the phosphor.

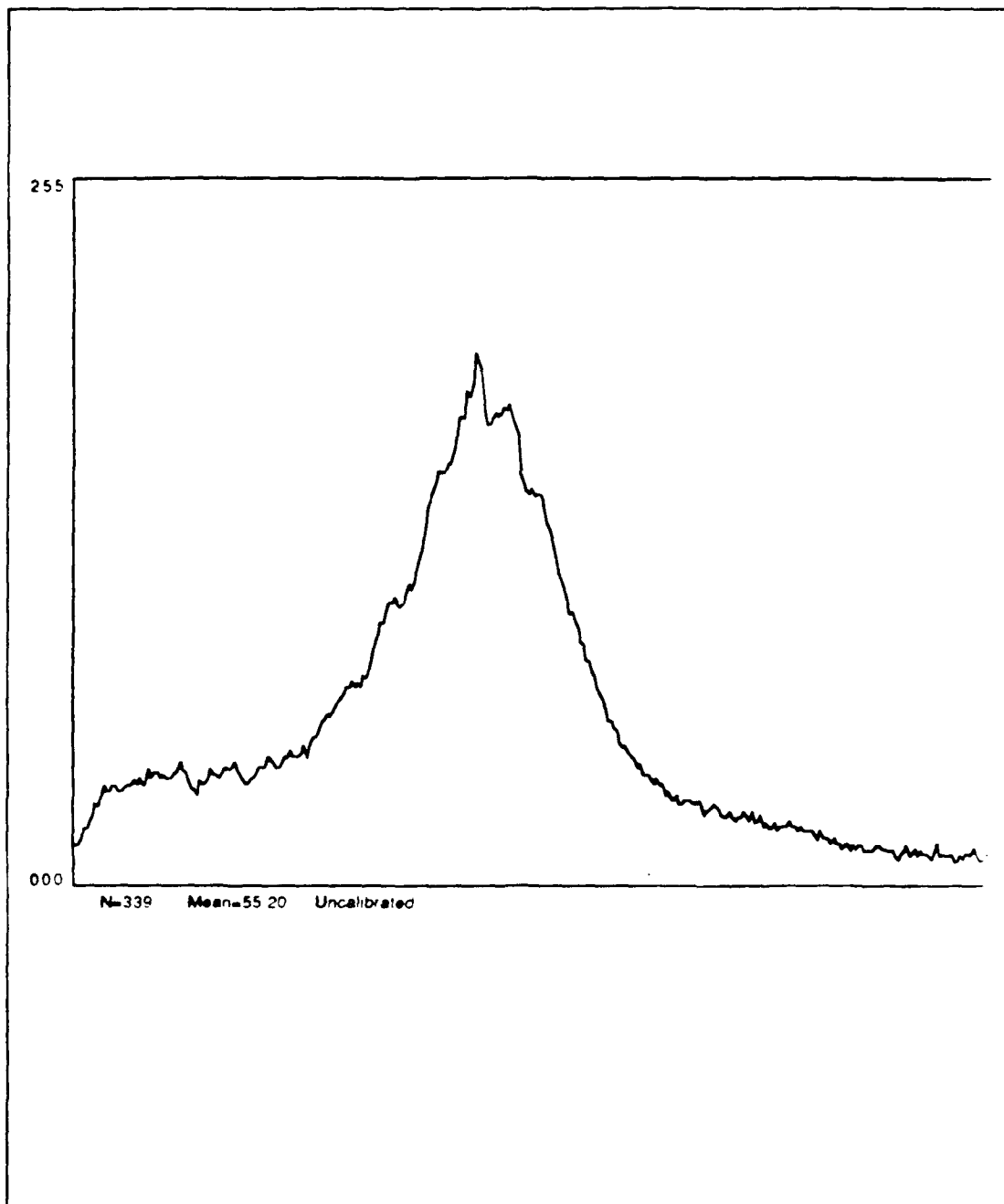


Figure 4. Representative Cut from Electron Beam Profile
from Front of Target Chamber.

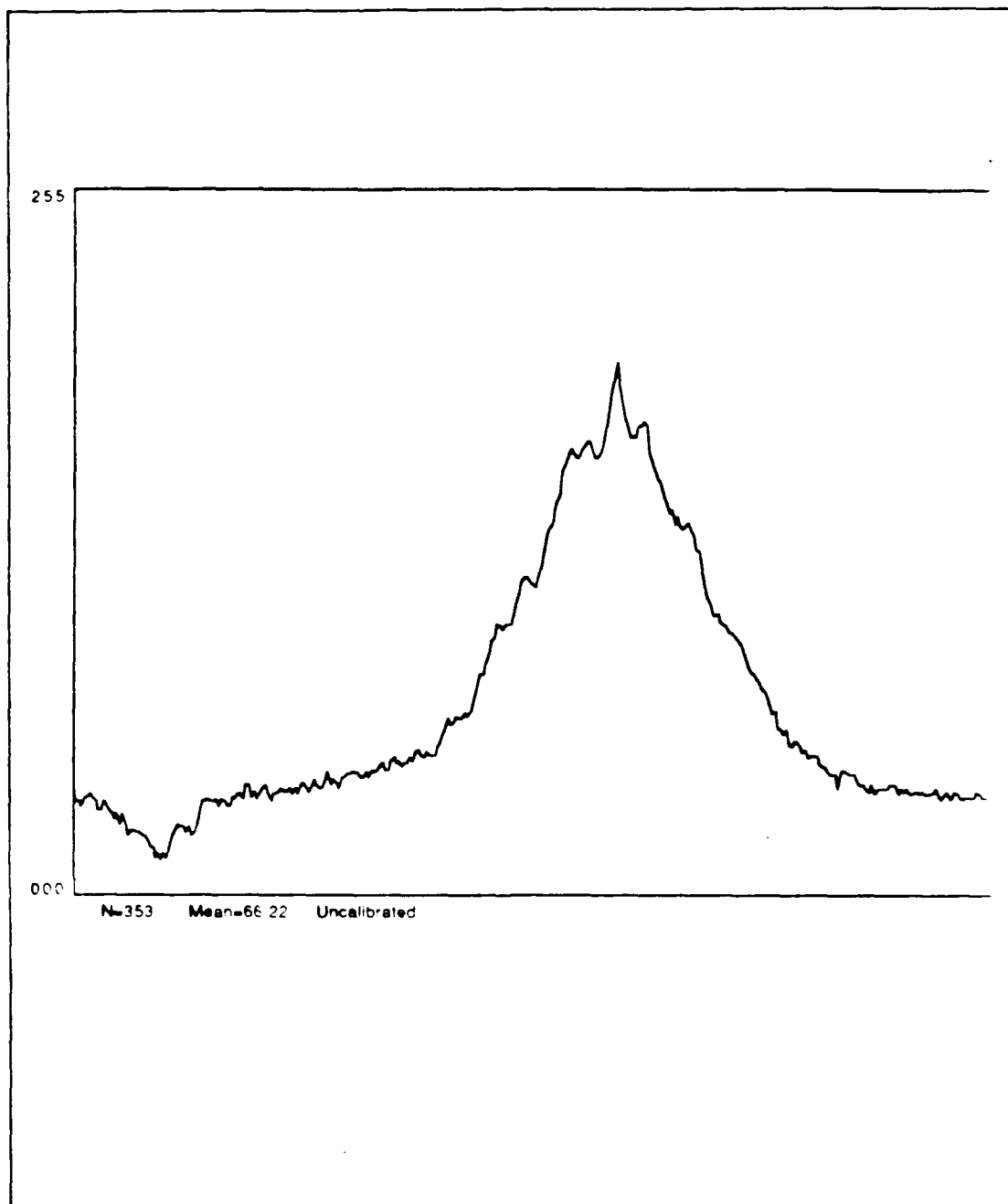


Figure 5. Representative Cut from Electron Beam Profile
from Back of Target Chamber.

Where $\rho(r)$ is the charge distribution, r is the radial distance off the axis and σ is defined by the radius at FWHM, $r_{1/2}$ as follows:

$$\sigma^2 = r_{1/2}^2 / 2 \ln 2 \quad (19)$$

Integrating over all space, it can be shown that the total charge within the electron beam (Q_T) is the following:

$$Q_T = \frac{\rho_0 \pi r_{1/2}^2}{\ln 2} \quad (20)$$

where $r_{1/2}$ is again the radius at FWHM and can be measured. Solving for ρ_0 and substituting into Equation (18), the beam profile becomes:

$$\rho(r) = \frac{Q_T \ln 2}{\pi r_{1/2}^2} e^{-\left(\frac{r}{r_{1/2}}\right)^2 \ln 2} \quad (21)$$

It can also be shown that the charge contained within the FWHM ($Q_{1/2}$) is equal to one half the total charge and it can be further shown that the average value of $\rho(r)$ for $r \leq r_{1/2}$ is:

$$\overline{\rho(r)} = \frac{\rho_0}{2 \ln 2} \quad (22)$$

This states that the average charge density over the range of the FWHM is approximately 72 percent that at the maximum intensity. Being certain that the Y123 samples were all within the FWHM during the entire irradiation time and knowing that half the total charge was within this same region, fluctuations in the beam and sample displacements off center can be accounted for by modeling an average electron beam of height $\rho(r)$ and of width $2r_{1/2}$ as seen in Figure 6.

The earlier assumption of discrete increments in the beam size may now be used to determine the beams' FWHM throughout the target chamber. Finally to calculate the fluence, the total charge determined earlier from the SEM can be adjusted to model the average electron beam and then divided by the correct beam area. This in turn, can be used to calculate the dose as described earlier. Tabulated data of the electron beam profile and parameters will be presented in the Results section.

To create the required defect density for effective flux pinning in Y123, approximately 3.6×10^{18} electrons per square centimeter were required. This was arrived at by the following expression obtained through unit analysis:

$$\phi = \frac{2DV}{N_o \sigma / A} \quad (23)$$

where ϕ represents the fluence, D is the defect density assumed to be approximately 10^{16} defects per cubic centimeter based on previous neutron experiments,

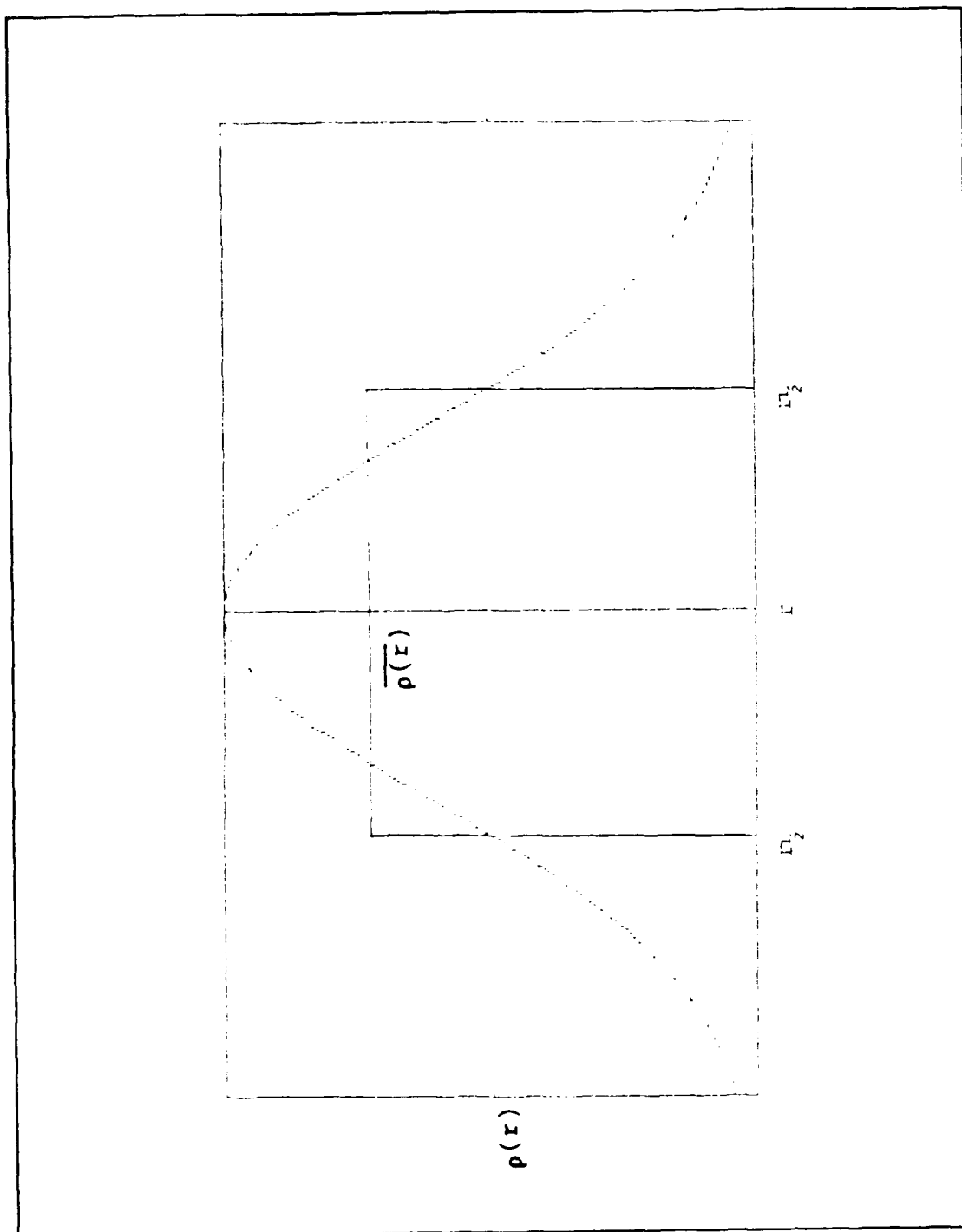


Figure 6. Electron Beam Model

V is the sample volume assumed to be approximately 0.3 cm³, N_0 is Avogadro's constant, σ is the electron nuclear cross section for oxygen recoil assumed to be approximately 50 mb and A is the atomic number of oxygen [Ref. 18]. Oxygen is used because by inspection of the weighted collisional specific energy losses in Tables II and III, it clearly has the largest effect on nuclear recoil in the Y123 superconductor. The factor of 2 is due to the average electron beam as described earlier.

III. EXPERIMENTAL SETUP, PROCEDURES AND ANALYSIS

A. EQUIPMENT SETUP

This experiment was conducted at the Linear Accelerator (LINAC) located at the Naval Postgraduate School. A brief description is provided in Appendix A. Figure 7 shows the aluminum target chamber provided by the University of

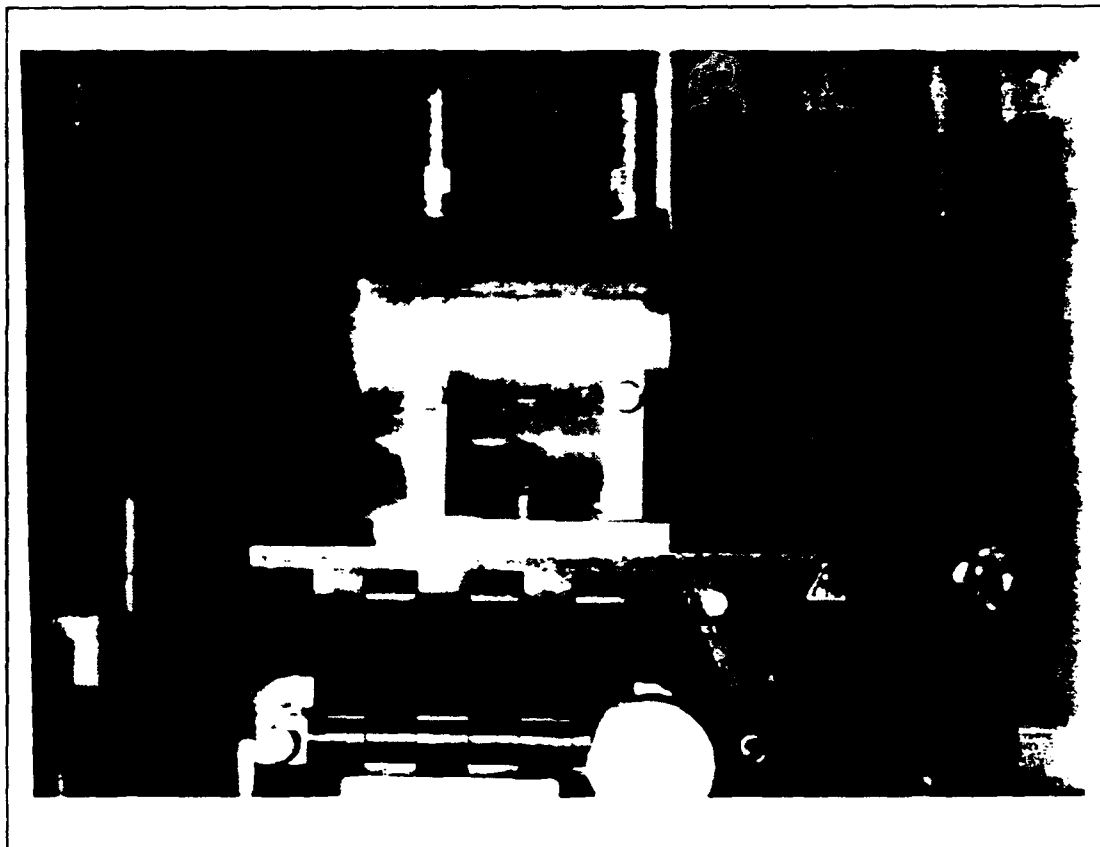


Figure 7. Aluminum Target Chamber Used for Holding the Irradiation Samples.

Houston. Because of the cylindrical shape, the sample holders were geometrically round and supported the Y123 samples for both runs. For the first run, several samples were placed on each plate, but as discussed earlier, all were within the FWHM of the electron beam. For the second run; however, it was decided to place one sample per plate located at the center. The chamber was designed to hold many plates or spacers as needed to fill the entire chamber. The front plate facing the electron beam was glass-beaded to provide a surface for OTR observation and a measured crosshair was inscribed at the center so that the beam size could be measured. Phosphor was put on the back outer plate and a similar crosshair was inscribed again for beam measurement. This can be seen by inspection of Figure 3, where the penciled crosshair inhibited phosphorescence.

Because a drastic decrease in T_c is observed when the concentration of oxygen vacancies increases [Ref. 13], a steady flow of ultra high pure oxygen was used throughout the target chamber in hopes that the flow would aid in annealing the Y123 samples. To allow for oxygen flow through the chamber, two hose attachments were located on the top of the chamber; one for an inflow and the other for an outflow. Likewise, the sample plates had holes through them so the oxygen could flow throughout the chamber. To prevent the oxygen from escaping, mylar windows were placed over both ends of the target chamber. The outlet hose end was submerged in a bucket of water to determine that oxygen was flowing through the target chamber by observing bubbles.

To ensure the electron beam passed through the center of the chamber, alignment of the target chamber with respect to the beam was crucial. Figure 8 shows a schematic of the target area. A ladder including a bull's-eye, a diffuse screen, a front surface mirror and a blank area was placed in the vacuum chamber. A laser was then positioned so that its light could travel through the vacuum chamber and to a benchmark located at the beam height. Through the use of the laser and ladder assembly the target chamber and SEM could be aligned.

The SEM was placed downstream of the target chamber and optical stands were used to support the sample chamber and SEM. After the alignment was finished and because of space constraints, mirrors were positioned so the beam could be monitored from the front and back of the target chamber. Figures 9 and 10 show the target chamber, SEM and mirrors set up as described above. To monitor the electron beam, video cameras were used to view the beam in the vacuum chamber, and the front and the back of the target chamber. Closed circuit television cameras were used at the vacuum chamber and back of the target chamber and a CCD camera (COHU model # 163241) was used for the front of the target chamber. The COHU, model # 163241) is a small, compact, solid state, monochrome charged coupled device (CCD) camera which is sensitive to low intensity light and used in OTR experiments [Ref. 19]. The outputs of the cameras

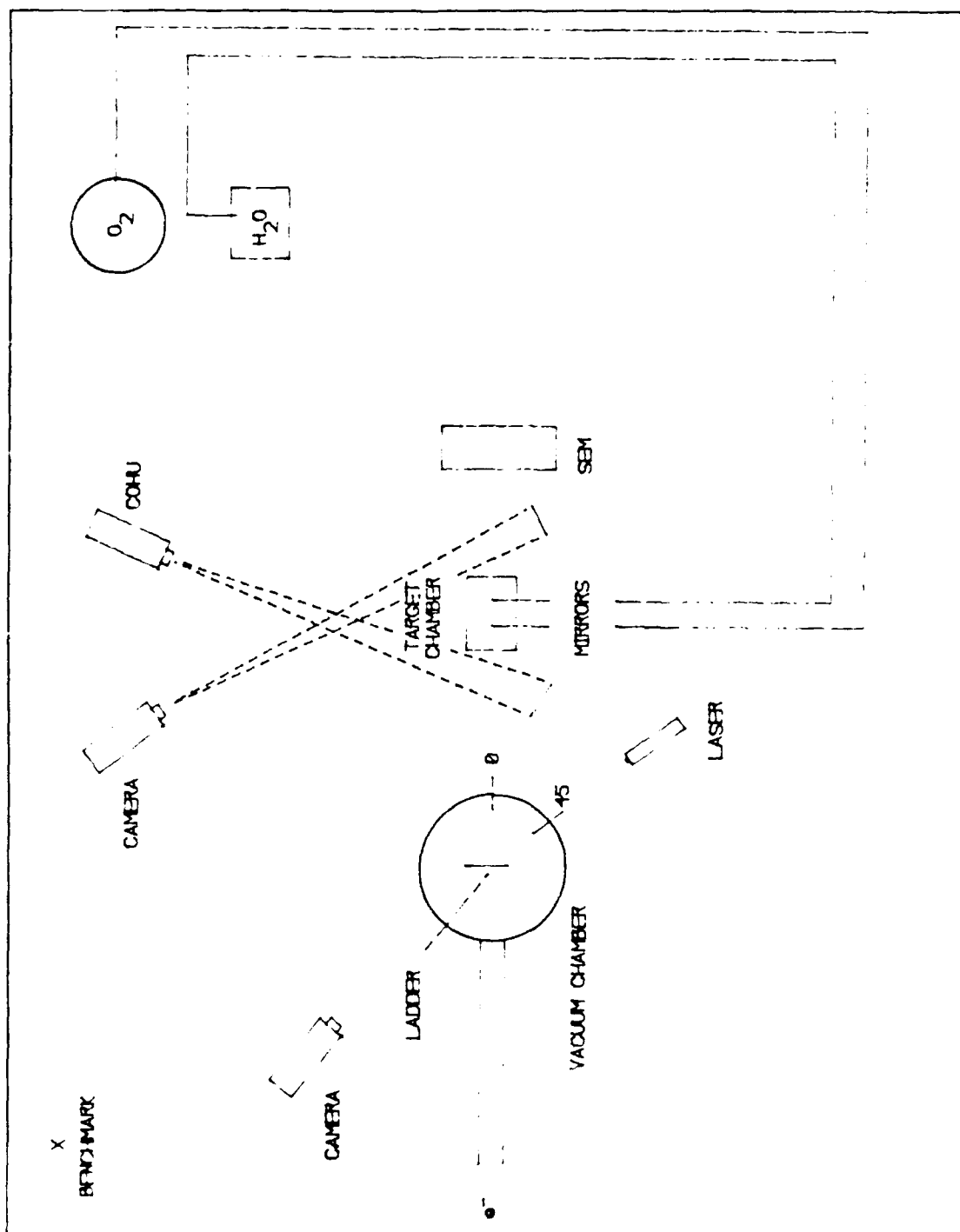


Figure 8. Target Area Setup

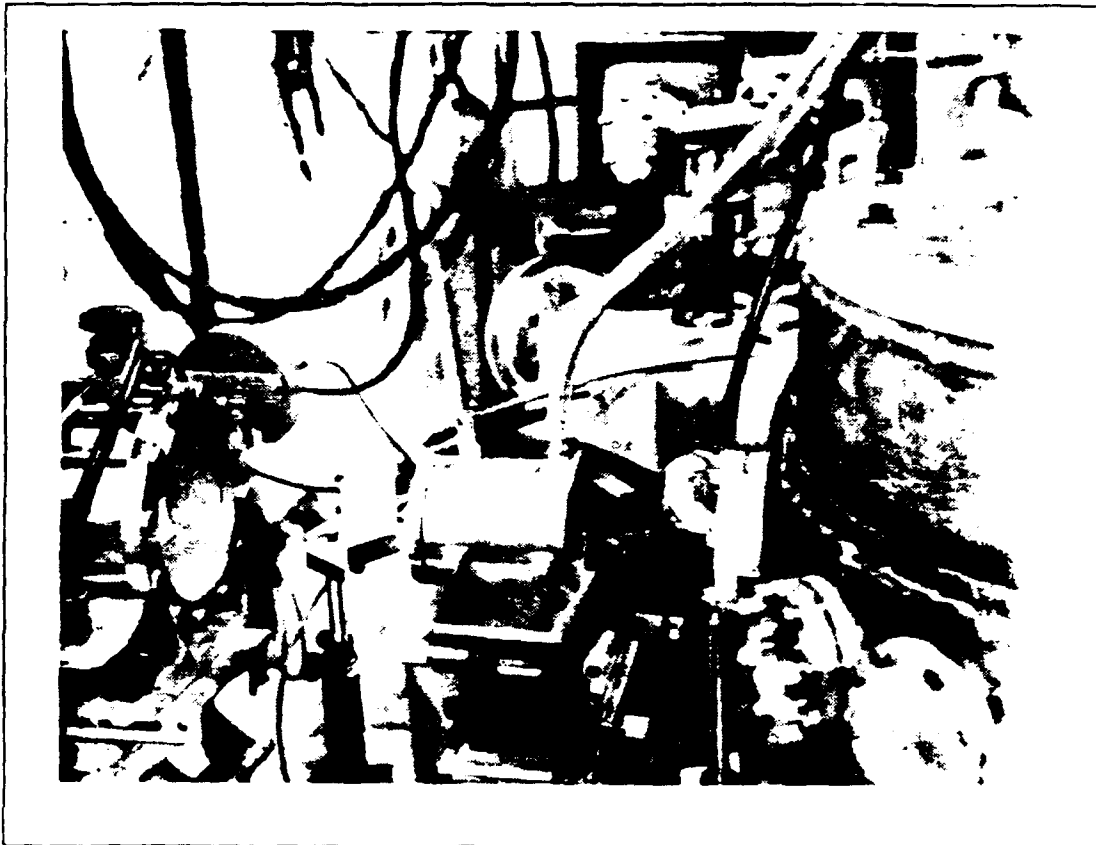


Figure 9. Target Chamber, SEM, and Mirrors (Side View).

were connected to video monitors and a frame grabber board in a MacIntosh computer for imaging in the control room.

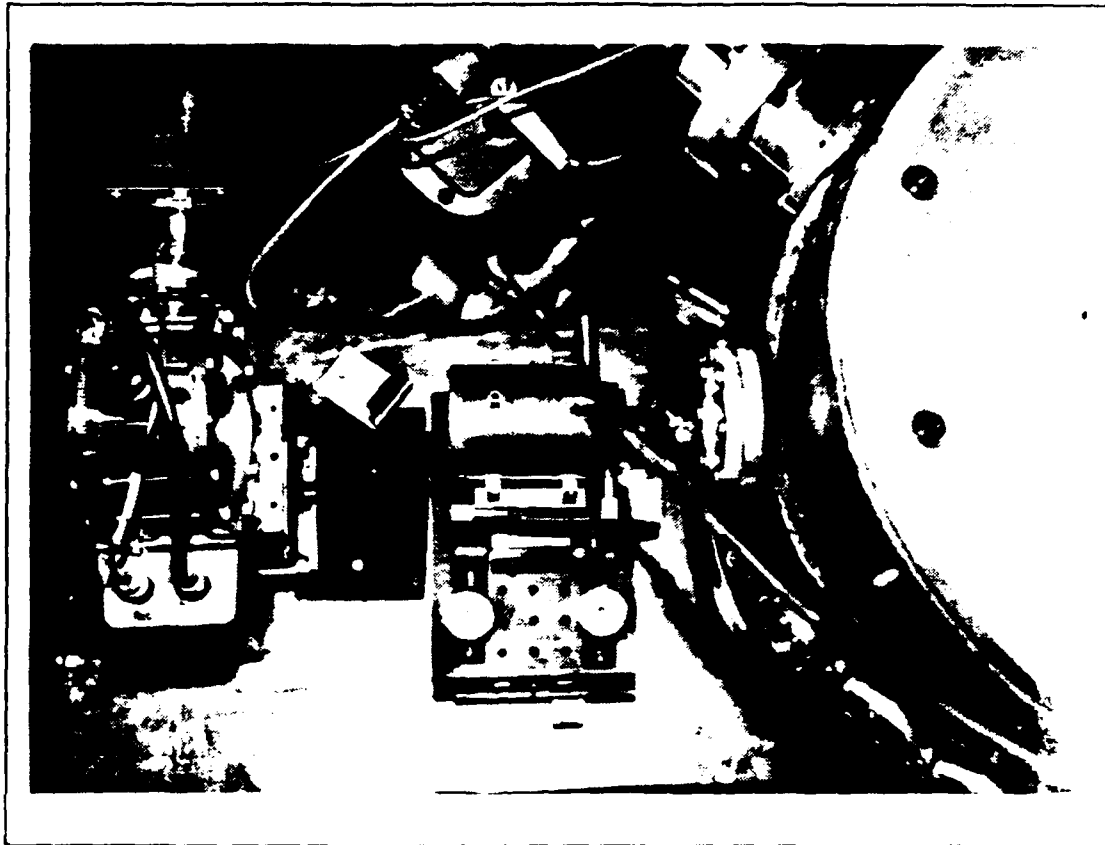


Figure 10. Target Chamber, SEM and Mirrors from Above.

B. PROCEDURE

1. ALIGNMENT

To ensure that the samples were irradiated by the electron beam, alignment of the target chamber with respect to the beam was critical. Required for this alignment was the ladder assembly and laser alignment. Once the ladder was assembled, a HeNe Laser was leveled and aligned through the center of the 45 degree port of the vacuum chamber and to a benchmark which was at the nominal electron beam height. The ladder was then placed in the center of the

vacuum chamber and positioned so that the mirror was aligned so that the laser beam reflected back on to itself. A stepping motor was used to rotate and move the ladder vertically up and down and the positions of reflection or "home" and heights of the bullseye, diffuse screen and the vacant space were recorded. The vacuum chamber was then closed and taken under a vacuum in preparations to align the target chamber and the SEM.

Now that the laser and the ladder assembly were aligned with respect to the electron beam, the target chamber and SEM could likewise be aligned simply by using the laser and ladder assembly. With the position of "home" known, the mirror was rotated 45 degrees and according to Snell's Law of Reflection, the reflected laser beam through the 0 degree port designated the electron beam trajectory. The SEM was aligned first as it was located downstream of the target chamber and because the aluminum foils in the SEM are very large in relation to the electron beam diameter, the alignment wasn't as critical as the chamber's. It was subsequently placed on a level optical stand at the height of the electron beam. The target chamber was then placed on another level optical stand upstream of the SEM. When the laser beam was seen through both, very, small, entrance and exit holes on the front and back faces of the target chamber respectively, the alignment was complete. With the front mylar window already in place, the sample chamber was then secured to the stand so that the sample plates could be interchanged and the back mylar window attached. Mirrors were

then placed so the front and back plates would be visible to their video cameras. To check and maintain alignment, an additional camera was positioned so it could view the ladder assembly, containing the scattering chamber's bull's-eye, through a port hole.

To insure that the electron beam's trajectory was the same as the laser's, the ladder was positioned so the bullseye was at the same height and perpendicular to where the electron beam should be. When the electron beam was turned on, a steering magnet was used to steer the beam so it hit the bull's-eye; therefore maintaining the electron beam alignment with the laser the target chamber and SEM.

2. Irradiation

Prior to the irradiation, dosimetry was conducted to establish the required voltage-dose relationship. Five TLD's were exposed to the electron beam for the second run but for the first run, the dosimetry was put off due to time constraints until after the run was complete. Due to a mechanical breakdown of the LINAC, the dosimetry was never done for the first run.

To examine the full effects of electron irradiation on Y123 superconductors, it was necessary to examine a wide range of fluences up to the required value of 3.6×10^{18} electrons per cm^2 . The sample plates, with the samples already mounted, were positioned in the target chamber with the glass beaded plate on the front surface facing foreword and the phosphor covered plate on the back surface

facing downstream. The back mylar window was installed and the electron beam alignment was verified one last time prior to the irradiation. A current integrator from the SEM was used on the first run to obtain the charge whereas a voltage integrator was used for the second run. Throughout the experiment, the electron beam profile images were captured on a computer for real-time analysis and were also stored for a future and more careful review.

After the irradiation was complete for all the samples, the target chamber and samples were allowed to "cool" down until the surface was <2 mRem per hour on contact, prior to their analysis. This took between 15 minutes for those samples which received less than 0.05 percent of the required fluence to 2 days for those which received the maximum percentage of 71.

C. ANALYSIS

1. Identification

Identification was done so the radioactive isotopes produced as a result of the radiation could be identified and their activities calculated. This was important because the samples had to be shipped to the University of Houston and the types and amount of radiation determines the method of shipment. Identifying the radioactive isotopes after a radiation experiment also adds to the information gained as a result of the experiment and assists in a more thorough understanding of the irradiation. After the samples had cooled down sufficiently,

an energy spectrum was obtained for each Y123 sample using a Na-I(Tl) scintillator and a Nucleus Pulse Height Analyzer (PHA) and compared to an energy calibration for their identification. The PHA was calibrated using a three point calibration consisting of standard Co57, Co60 and Cs137 sources. Knowing the target elements and possible nuclear reactions I had a very good idea of which radioactive isotopes might be present. To obtain a "clean" energy spectrum; I acquired a background spectrum for the same time period of each of the sample energy spectrums, 5 minutes, then subtracted the background from the Y123 spectrum.

Because the samples were in two groups; one being a single crystalline Y123 sample and the other being a single crystalline Y123 sample with plastic supports, a silver base paste and silver leads for measuring the resistance, there were two distinct energy spectrums. Figure 11 shows the spectrum of the pure samples prior to the background subtraction, Figure 12 shows the background energy spectrum in which a peak at 1460.8 keV identified as K40 can be seen. Figure 13 shows the spectrum of the pure samples with the background subtracted. This spectrum was easily analyzed; whereas Figure 14 shows the energy spectrum of the samples with leads, supports, etc... after the background was subtracted. The complexity of this spectrum as compared to the earlier one lead to difficulties in identifying the subsequent energy peaks because although I had an idea of which radioactive isotopes may be present, not all the additional peaks were isotopes of

silver and aluminum. Therefore, I had to assume there were accidental coincidences or sum peaks present.

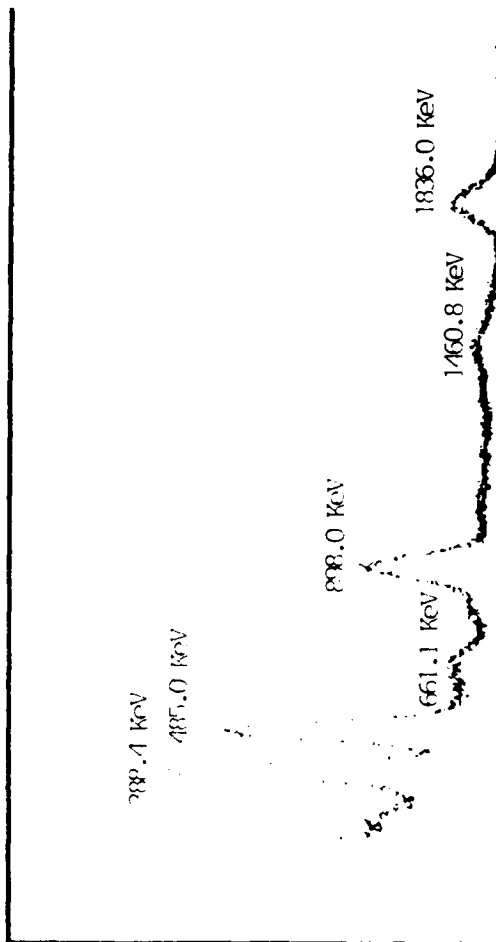
When gamma rays are emitted from a radioactive source, they enter a scintillator, in this experiment a Na-I (Tl) scintillator was used, and their kinetic energy is converted to detectable light through photons. A photomultiplier tube, through photoelectric absorption, converts the photons into electrons, and as the number of electrons change, a current is produced which takes the shape of a pulse. The amplitude of the pulse which is directly related to the corresponding charge generated, produces a single peak which appears at the total electron energy corresponding to the energy of the incident gamma rays.

Additional peaks caused by the coincident detection of two or more gamma ray photons may also appear in the recorded pulse height spectrum. This summation process involves multiple radiations from the same nuclear decay event and is known as a true coincidence. However, another process can also lead to summed pulses due to the accidental combination of two separate events from independent decays if they occur within the "dead" time or resolving time of the system. These chance coincidences may even occur in the absence of true coincidences and when multiple radiations are involved, accidental sum peaks may occur at all possible combinations of any two single energies. The following relation can be used to assist in identification of any potential sum peaks:

FEB 08 1991 10:39:22 AM MODES: PHA ADD % DEAD TIME: 00
 GROUP: H1 US: 1K CTS GAIN: 4096 CHLS OFFSET: 0000 CHLS ID: A14

Nuclaus

F1	F2	ERASE
F3	F4	SETUP
F5	F6	COLOR
F7	F8	OUTLAP
F9	F10	MORE



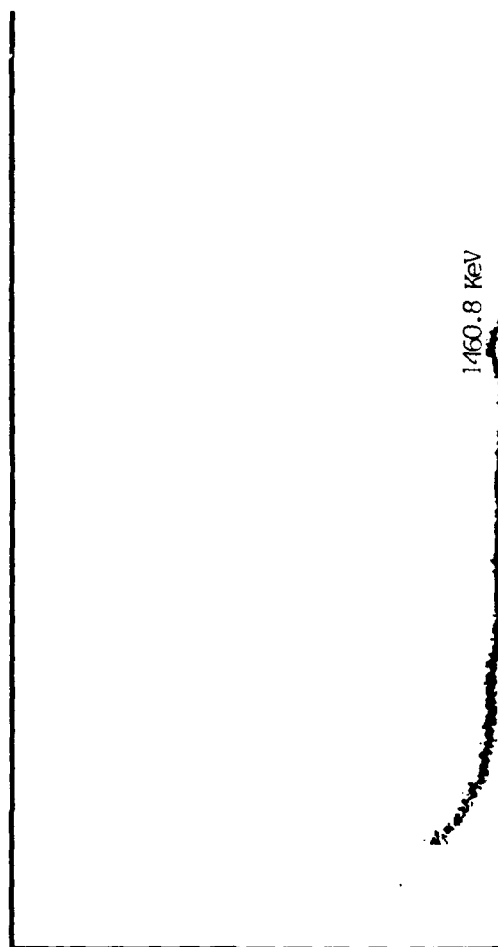
CHANNEL: 0000 COUNTS: 00000000 REGION OF INTEREST: OFF
 PK #: 00 CTDR: 0.00000 CHL FUIM: 0.00000 CHL GROSS: 00000000 NET: 00000000
 TIME LIVE PRESET: 000000 ELAPSED: 000300 REMAINING: 00 SECONDS

Figure 11. Y123 Energy Spectrum with Background.

FEB 08 1991 12:39:41 PM MODES: **PIA ADD** % DEAD TIME: 00
 GROUP: H2 VS: 1K CTS GAIN: 4096 CHLS OFFSET: 0000 CHLS ID: BACKGROUND

Nucleus

F1	F2
ACOU	ERASE
F3	F4
GROUP	SETUP
F5	F6
ROI	COLOR
F7	F8
TRANS	OVLAP
F9	F10
EXPND	MORE



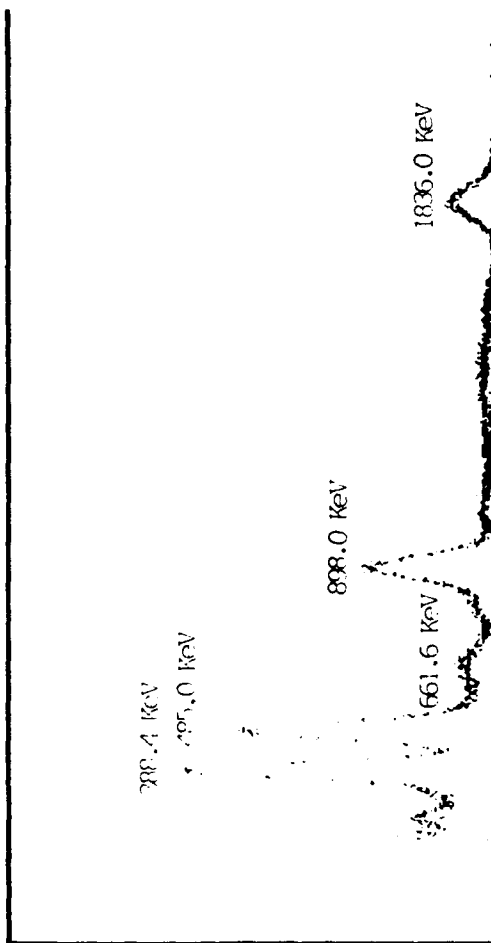
CHANNEL: 0000 COUNTS: 00000000 REGION OF INTEREST: OFF
 PK #: 00 CTDR: 0.00000 CHL FWHM: 0.00000 CHL GROSS: 00000000 NET: 00000000
 TIME LIVE PRESET: 000000 ELAPSED: 000000 REMAINING: 00 SECONDS

Figure 12. Background Energy Spectrum.

FEB 08 1991 10:39:22 AM MODES: PHA ADD % DEAD TIME: 00
 GROUP: H1 US: 1K CTS GAIN: 4096 CHLS OFFSET: 0000 CHLS ID: A14-BACKGROUND

Nucleus

F1	F2
ACOU	ERASE
F3	F4
GROUP	SETUP
F5	F6
ROI	COLOR
F7	F8
TRANS	OVLAP
F9	F10
EXPND	MORE



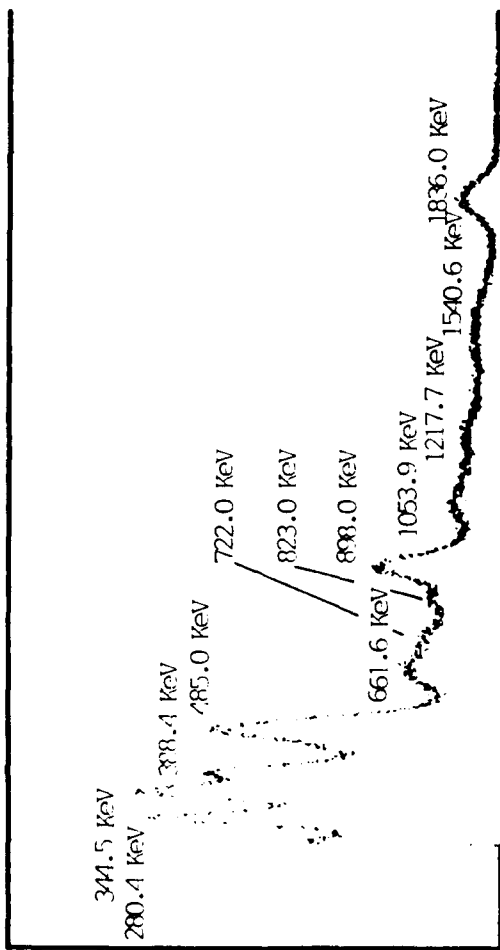
CHANNEL: 0000 COUNTS: 00000000 REGION OF INTEREST: OFF
 PK #: 00 CIRD: 0.00000 CHL FWHM: 0.00000 CHL GROSS: 000000000 NET: 000000000
 TIME LIVE PRESET: 000000 ELAPSED: 000300 REMAINING: 00 SECONDS

Figure 13. Y123 Energy Spectrum with No Background.

FEB 08 1991 12:05:27 PM MODES: **PHA** **ADD** % DEAD TIME: 00
 GROUP: H1 US: 2K CTS GAIN: 4096 CHLS OFFSET: 0000 CHLS ID: 115-BACKGROUND

Menu

F1	F2
ACQU	ERASE
F3	F4
GROUP	SETUP
F5	F6
ROI	COLOR
F7	F8
TRANS	OUTLAP
F9	F10
EXPND	MORE



CHANNEL: 0000 COUNTS: 00000000 REGION OF INTEREST: OFF
 PK #: 00 CIRD: 0.00000 CHL FWHM: 0.00000 CHL GROSS: 00000000 NET: 00000000
 TIME LIVE PRESET: 000000 ELAPSED: 000300 REMAINING: ∞ SECONDS

Figure 14. Y123 with Leads, Support, etc. . . .
 Energy Spectrum with No Background.

$$N_r = N_1 N_2 (\rho_1 + \rho_2) \quad (24)$$

where N is the net area of the peak divided by the acquisition time, ρ is the resolving time and the subscripts R, 1 and 2 imply random peak and the two possible summing peaks in question respectively [Ref. 20]. In this experiment, only one scintillator was used, therefore Equation (24) becomes:

$$A_r = \frac{2A_1 A_2 \rho}{t} \quad (25)$$

where A is the net area of the peak, ρ is the resolving time, t is the acquisition time, or the time it took to acquire the data in seconds, and the subscripts R, 1 and 2 hold the same meaning as before.

The resolving time for a Na-I (Tl) scintillator is 230 ns [Ref. 21]; however, in anticipation of added dead time in the photomultiplier tube and the electronics of the computer system running the PHA software, repeated calculations were made of the resolving time using Co60 because of its prominent sum peak, and the result was:

$$\rho = 7500 \pm 4500 \text{ n sec} \quad (26)$$

Even with this information however; not all the energy peaks of the complex energy spectrum could be identified. More importantly; however, all the peaks

from the samples by themselves were identified and a summary is contained in the Results section.

2. Activity

Another extremely important aspect of any irradiation experiment is the ability to determine the amount of radiation present after the irradiation. Once the energy lines of the radioactive isotopes are identified, the activity can be obtained by the following relationship:

$$A_1 = \frac{RATIO_1}{RATIO_{SOURCE}} \times A_{SOURCE} \quad (27)$$

where A denotes the activity (Ci), the subscript 1 denotes the isotope line in question, the subscript source denotes a reference source which is close in energy to the isotope in question, and the ratio is defined as follows:

$$RATIO = \frac{PeakCount - BackgroundCount}{AcquisitionTime} \quad (28)$$

The ratio of the source was obtained independently of the Y123 samples and the activities were tabulated from a reference set and corrected for their decay. The results of these calculations are tabulated in the Results section.

IV. EXPERIMENTAL RESULTS

A. RESULTS

The voltage-dose conversion plot (Figure 1) produces the following linear relationship:

$$DOSE_{CaF_2} = 2.7 \pm 0.5 \times 10^6 \frac{RADS}{VOLT} \times [V] \quad (29)$$

where [V] is the recorded SEM voltage from the voltage integrator from run 2. Using the values for (dE/dx) for run 2 from earlier, the measured dose, Equation (16), becomes:

$$DOSE_{MEAS} = 2.5 \times 10^6 \frac{RADS}{VOLT} \times [V] \times \left(\frac{D_1}{D_2} \right)^2 \quad (30)$$

and the calculated dose due to collisional energy losses becomes:

$$DOSE_{CALC} = 2.1 \frac{MeV}{gm/cm^2} \times \phi \times 1.6 \times 10^{-8} \frac{RADS \cdot gm}{MeV} \quad (31)$$

where ϕ is the fluence, corrected for the electron beam model expressed in electrons/cm².

The results of the electron beam profile analysis containing the beam area, fluence and calculated dose for the first run are tabulated in Table IV and analysis for the second run containing the electron beam area, fluence, calculated and the measured dose as well as a comparison between the two is contained in Table V.

TABLE IV
BEAM PROFILE ANALYSIS FOR RUN 1
(BEAM DIAMETER, FLUENCE AND CALCULATED DOSE)

ENERGY: 88.5 MeV						
PLATE	BEAM DIAMETER ±0.001 CM	SAMPLE	FLUENCE (el/cm ²) (±12%)	% REQ'D FLUENCE	IRRADIATION TIME (SEC)	CALCULATED DOSE (Rads x 10 ¹⁰) (±12%)
1	0.345	I20	2.5x10 ¹⁸	70.6	147,720	8.5
		I9	2.5x10 ¹⁸	70.6	147,720	8.5
2	0.362	I22	2.3x10 ¹⁸	64.2	147,720	7.8
		I27	2.3x10 ¹⁸	64.2	147,720	7.8
3	0.380	I32	2.1x10 ¹⁸	58.3	147,720	7.0
		I33	2.1x10 ¹⁸	58.3	147,720	7.1
4	0.397	I21	1.9x10 ¹⁸	53.3	147,720	6.4
		I23	1.9x10 ¹⁸	53.3	147,720	6.4
5	0.414	I30	1.8x10 ¹⁸	49.2	147,720	6.0
		I31	1.8x10 ¹⁸	49.2	147,720	6.0
6A	0.432	I14	4.6x10 ¹⁷	12.9	48,900	1.6
		I17	4.6x10 ¹⁷	12.9	48,900	1.6
6B	0.432	I10	1.2x10 ¹⁸	32.2	98,820	3.9
		I15	1.2x10 ¹⁸	32.2	98,820	3.9
7	0.448	TEM	1.5x10 ¹⁸	41.9	147,720	5.1
EXIT	0.466	----	----	----	----	----

**TABLE V. BEAM PROFILE ANALYSIS FOR RUN 2
(BEAM DIAMETER, FLUENCE, CALCULATED AND MEASURED DOSE
WITH DOSE DETERMINATION COMPARISON).**

ENERGY: 92.0 MeV								
PLATE	BEAM DIAMETER ± 0.001 CM	SAMPLE	FLUENCE (el/cm^2) ($\pm 12\%$)	% REQ'D FLUENCE	IRRADIATION TIME (SEC)	CALCULATED DOSE (Rads) ($\pm 12\%$)	MEASURED DOSE Rads ($\pm 10.0\%$)	% DEVIATION
1	0.500	A14	8.7×10^{16}	2.4	51,420	2.9×10^9	2.4×10^9	17.2
2	0.509	A16	8.4×10^{16}	2.3	51,420	2.8×10^9	2.3×10^9	17.9
3	0.518	A15	8.1×10^{16}	2.2	51,420	2.7×10^9	2.2×10^9	18.5
4	0.526	A12	7.8×10^{16}	2.2	51,420	2.6×10^9	2.2×10^9	15.4
5	0.535	T2	1.5×10^{15}	0.04	1,200	5.0×10^7	4.1×10^7	18.0
6A	0.544	T14	1.5×10^{15}	0.04	1,200	5.0×10^7	4.0×10^7	20.0
6B	0.544	T15	1.4×10^{16}	0.4	10,080	4.7×10^8	3.8×10^8	19.2
7	0.552	T17	7.1×10^{16}	2.0	51,420	2.4×10^9	2.0×10^9	16.7
8	0.561	T6	6.9×10^{16}	1.9	51,420	2.3×10^9	1.9×10^9	17.4
		Positron	6.9×10^{16}	1.9	51,420	2.3×10^9	1.9×10^9	17.4
EXIT	0.570							

Due to the electron beam model of an average charge density, the error percentage for the number of electrons incident on the Y123 samples and subsequently the fluences reported are estimated to be $\pm 12\%$; hence, the error associated with the calculated dose is also $\pm 12\%$. Due to the error associated with the electron beam diameter and linear regression for the voltage-dose conversion plot, the error percentage for the measured dose is $\pm 10\%$. Of interesting note however, the average deviation between the calculated and measured dose is $17.8 \pm 0.4\%$. This deviation is not too far different from the measured dose considering the uncertainties involved.

In comparing the electron beam for both runs of this experiment, the 88.5 MeV run produced a beam with FWHM's between 3.45 and 4.66 mm whereas the 92.0 MeV run produced FWHM's ranging between 5.10 and 5.70 mm. There is insufficient data however, to draw any conclusions about the dependence of the electron beam size on the electron energy. The maximum fluence obtained was $2.5 \pm 0.6 \times 10^{18}$ electrons/cm² which corresponded to a dose of 8.5×10^{10} rads. This differs from our reported maximum value of $3.6 \pm 0.6 \times 10^{18}$ electrons/cm² as contained in Appendix D by $1/(2 \ln 2)$. This thesis contains a more accurate model of the electron beam and accounts for the discrepancy.

Tables VI and VII show the identification summary and radioactive isotope activity totals respectively for the second run. The Y123 samples of the first run were not analyzed with a PHA. Those energies identified with a "?" indicate an undetermined identification.

The results of the University of Houston's analysis of the high temperature superconductor samples are contained in Appendix D, a copy of our submission to Applied Physics Letters.

TABLE VI. IDENTIFICATION SUMMARY [REF. 22]

ENERGY (KeV)	ID	REACTION
280.4	Ag105	Ag107 (e,2n) Ag105
344.5	Ag105	Ag107 (e,2n) Ag105
388.4	Y87	Y89 (e,2n) Y87
485.0	Y87	Y89 (e,2n) Y87
661.6	Cs137	Ba138 (e,p) Cs137
722.0	SUM	Ag105 (344.5) + Y87 (388.4)
823.0	?	?
898.0	Y88	Y89 (e,n) Y88
1053.9	?	?
1217.7	?	?
1460.8	K40	BACKGROUND
1540.6	?	?
1836.0	Y88	Y89 (e,n) Y88

TABLE VII. RADIOACTIVE ISOTOPE ACTIVITY

ISOTOPE	ACTIVITY (2/8/91)	HALF LIFE
Ag105	0.5 n Ci	41.3 days
Y87	50 n Ci	80.3 hours
Cs137	0.3 μ Ci	30.17 years
Y88	1 μ Ci	106.6 days

B. CONCLUSIONS

The results of this experiment provide a methodology for irradiation experiments at the LINAC such that the fluence and dose can be determined, the products of the irradiation identified, and their activities calculated. These results will offer a more complete understanding of future irradiation experiments from the beginning to the end of the irradiation. The results show two consistent methods of determining the dose on a target which in turn may be used as a measure of the irradiation.

An instrumental factor in determining the fluence and dose on a Y123 sample was monitoring the electron beam. Monitoring the electron beam using OTR and phosphorous provided immediate analysis for rough determinations of the fluence and dose. The saved electron beam profile images also proved to be invaluable for more thorough analysis. OTR proved to be a better beam diagnostic than phosphorescence because the phosphorescence, over time, "died". Also, the phosphorescence, being initially very intense, was apt to burn a hole in remote monitors; whereas the OTR did not. By analyzing the electron beam's profile, an accurate model was developed for a more in depth knowledge of the charge distribution and beam area. As a result, the information obtained from the electron beam's location and profile provided critical information concerning the fluence and dose.

Table V shows the consistency between the two methods of determining the dose. This is significant because now, after minor preliminary calculations, a fairly accurate (+/- 17.8 %) determination of the dose on a target can be done at any time during an experiment. Furthermore, the method of alignment presented can be used for all experiments conducted at the Linear Accelerator at the Naval Postgraduate School.

Post irradiation analysis was also conducted on the Y123 samples and the radioactive isotopes produced were identified and their activities were calculated. From Table VI, the radioactive isotopes produced as a result of electron irradiation on a Y123 sample are Y87, Y88 and Cs137. It was found that the primary background radiation peak in the nuclear radiation laboratory at the Naval Postgraduate School is K40. Even though other isotopes are listed and are important for analysis here, they will change depending on how the samples are mounted to other materials. It was also determined that Y88 had the highest activity at the experiments conclusion (1 Ci); however, taking into account the half lives it can be seen that Cs137 will have the highest residual activity.

The conclusions of the effects of high energy electron irradiation on Y123 are contained in Appendix D. Of worthy note is the manner in which the effects of the irradiation on critical current enhancement were studied. The average primary knock-on recoil energy, \bar{E}_p , produced by different types of radiation was found to be related to the defect size and is approximately 100 eV for the target

atoms of yttrium, barium, copper and oxygen. Because it was determined that the defect size played a vital role in critical current enhancement, this proved to be an excellent measure of the irradiation. Recall that in my dose calculations, the radiative losses were neglected. Therefore, as the dose is a measure of the collisions and ionization, the average primary knock-on recoil energy is a measure of Bremsstrahlung radiation; and hence, two measures of the irradiation are presented.

In summary, the methods presented in this paper can be used as a reference for use in future irradiation experiments.

C. RECOMMENDATIONS

Recommendations stemming from this experiment and research include:

- (1) Dosimetry should be conducted, with at least ten unsaturated TLD readings prior to every irradiation experiment.
- (2) Prior to any shipment of irradiated samples, an analysis should be conducted to identify the radioactive isotopes and calculate their associated activities. This should be planned for, so that time restraints are not encountered.
- (3) A library of energy spectra should be obtained to help in identifying energy peaks.
- (4) OTR should be used over a phosphorous screen if at all possible.

APPENDIX A - LINAC CHARACTERISTICS

This accelerator is a traveling wave type which consists of three ten foot sub-accelerators, each powered by a klystron amplifier which delivers up to 22 megawatts peak power. The RF pulse length is 3.5 microseconds, repeated 120 times per second. The electrons are injected at 80 kilovolts and exit the accelerator at up to a maximum of 120 MeV. An average electron current of less than 1 microamp is obtained. The beam energy used was 88.5 MeV and 92.0 MeV for runs 1 and 2 respectively. Figure A1 depicts the LINAC at the Naval Postgraduate School [Ref. 1].

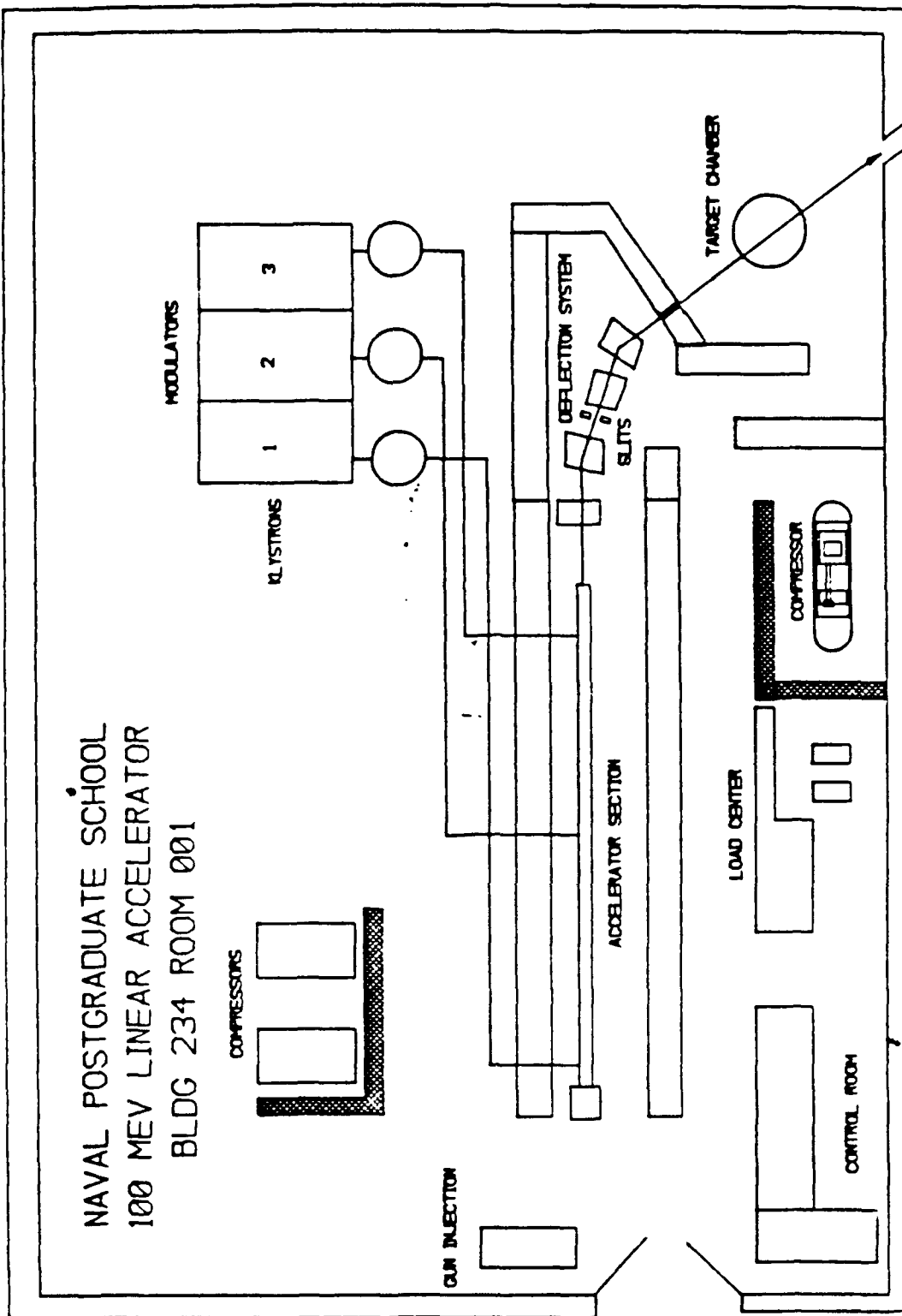


Figure A1. LINAC Equipment Layout

APPENDIX B - SEM CALIBRATION

Prior to the irradiation experiment, it was determined that a calibration of the SEM was necessary in order to determine the number of electrons incident on the Y123 samples. A faraday cup was placed in the electron beam path downstream of the SEM. Because the aluminum foils in the SEM are incapable of stopping the incident electrons, the electrons would travel downstream until hitting the faraday cup, which is made of lead. Under a vacuum, the faraday cup would stop the electrons. An efficiency of the SEM could be calculated by comparing the charge accumulated in the SEM to the charge accumulated in the faraday cup. It was not feasible to use the faraday cup in the present experiment due to space constraints in the target room.

Three experiments were done to calculate the SEM efficiency. The first experiment was to see if the efficiency of the SEM was dependent on the current integrators connected to the SEM and the faraday cup. Once it was established that the SEM efficiency was not dependent on the current integrator being used, the second experiment was to determine the effects on the SEM efficiency by changing both the electron beam current and energy. The third experiment to determine the SEM efficiency was to see if any of the secondary electrons produced at the SEM contributed at all to the charge determined in the faraday

cup. The results of all three experiments were then compared to determine the overall SEM efficiency.

The two current integrators used for the first experiment were a BIC and a Keithley integrator. At 88.5 MeV one run was conducted with the SEM connected to the BIC and the faraday cup connected to the Keithley, then the leads were switched and the integrators reversed for another run at the same energy. The results were identical. Regardless of the integrator used, the current in the SEM was 1.27×10^{-8} Amperes and the current in the faraday cup was 1.00×10^{-7} Amperes resulting in an SEM efficiency of 12.7 %.

Once it was established that the integrators used for the SEM and the faraday cup had no effect on the efficiency, the effects of varying the electron beam's current and energy were studied. By using the current obtained from the faraday cup as the true electron beam current and by subsequently changing the current, the efficiency as a function of current was calculated. Because the first experiment was conducted at 88.5 MeV and at 1.0×10^{-7} Amperes, ten runs were conducted at 88.5 MeV at three currents other than the one used in the first experiment. Similarly, eight runs were conducted at 1.0×10^{-7} Amperes at three energies other than the one used in the first experiment.

For the third experiment, a magnet was placed in the end station of the LINAC target chamber to sweep out the secondary electrons produced in the SEM to determine if they had any effect on the faraday cup. Two runs were conducted

at 88.5 MeV and 1.0×10^{-7} Amperes and the results were consistent with the efficiency being calculated at 12.7 % and 12.8 %. The secondary electrons had no effect on the faraday cup. Tables B-I and B-II summarize the three experiments and are plotted in Figures B1 and B2 respectively.

**TABLE B-I. SEM EFFICIENCY VS. ELECTRON BEAM CURRENT
AS MEASURED WITH FARADAY CUP**

E=88.5 MeV	
ELECTRON BEAM CURRENT (A)	SEM EFFICIENCY
1.40×10^{-8}	13.1/12.5/13.3
3.70×10^{-8}	12.1/12.2/12.0
1.00×10^{-7}	12.7/12.7/12.7/12.8
1.27×10^{-7}	13.8/12.9/12.9/11.8

**TABLE B-II. SEM EFFICIENCY VS. ELECTRON BEAM ENERGY
AS MEASURED WITH FARADAY CUP**

I=1.00×10^{-7}	
ELECTRON BEAM ENERGY (MeV)	SEM EFFICIENCY
24.3	12.4/12.4/13.0
29.9	12.8/12.8/12.5
88.5	12.7/12.7/12.7/12.8
90.0	12.7/12.8

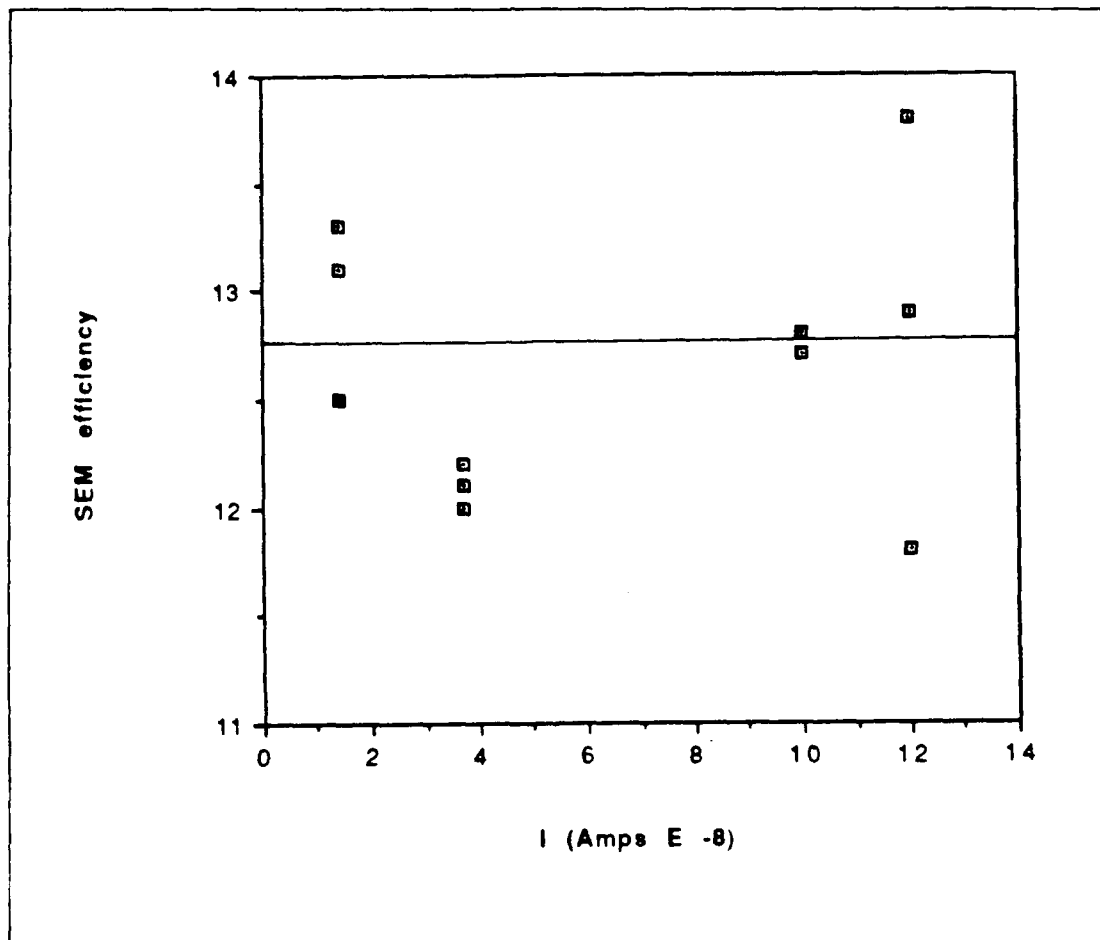


Figure B1. SEM Efficiency vs. Current as Measured with Faraday Cup at 88.5 Mev.

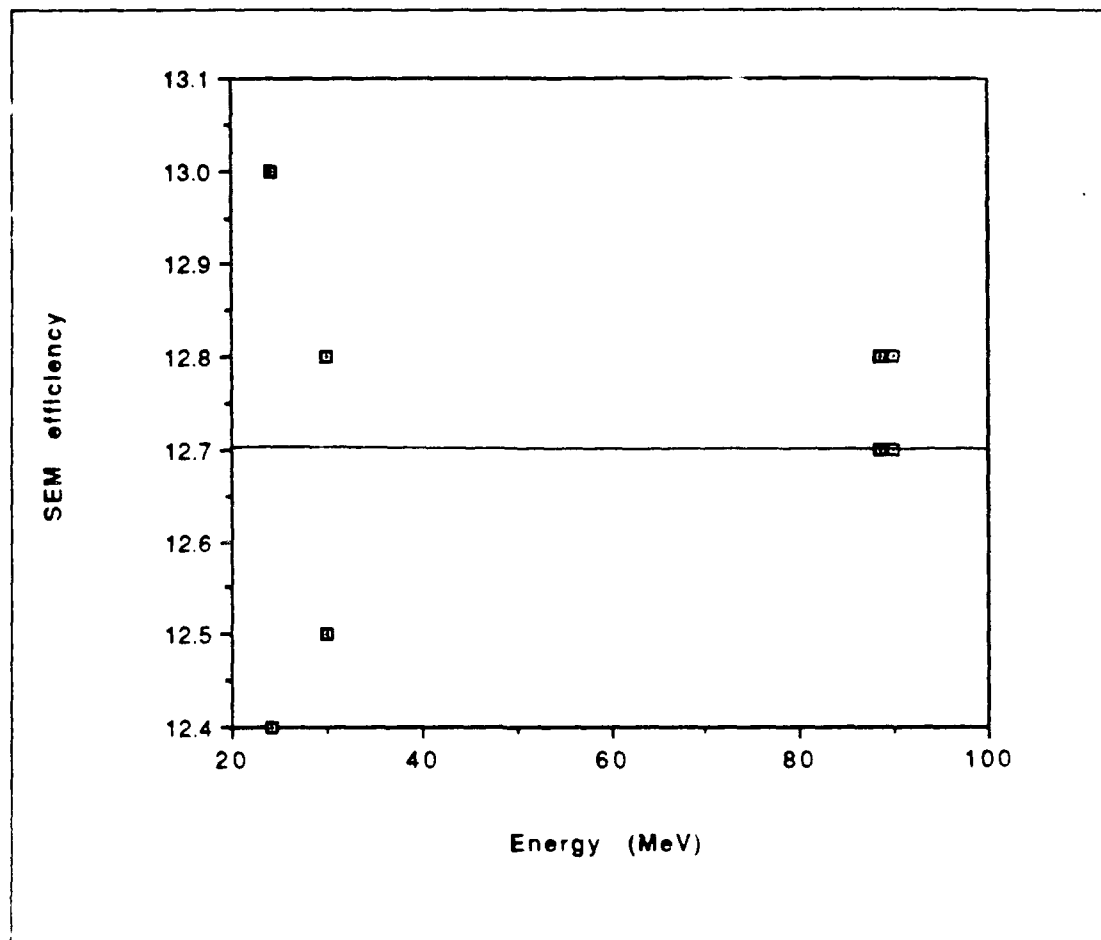


Figure B2. SEM Efficiency vs. Energy
as Measured with Faraday Cup at 1.0×10^{-10} Amps.

After analyzing the data, it was concluded that neither the integrators nor the secondary electrons effected the SEM efficiency calculation at all. It was also concluded, as can be seen by Figures B1 and B2, that the SEM efficiency was $12.7 \pm 0.5\%$ regardless of the electron beam current or energy. As a comparison, the SEM was removed and the faraday cup current was compared to the scattering

chamber toroid in the event that the SEM failed during the experiment. At 1.0×10^{-7} Amperes the toroid read 500 mV/cm. Using this relationship, the toroid could be used to determine the number of electrons incident on the Y123 samples. The SEM was then placed back in the electron beam path and the SEM efficiency and the toroid relationship were verified against the faraday cup at different electron beam currents.

APPENDIX C - SUPERCONDUCTOR THEORY

The phenomenon of superconductivity [Refs. 23,24,25] has intrigued the scientific community since its advent in 1911; and since the discovery of high temperature superconductors at liquid nitrogen temperatures in 1987, one just has to open any scientific journal to see numerous articles from around the world on this current "hot" topic. Superconductors have many unusual electromagnetic properties, and most applications take advantage of them. For instance, a superconductor exhibits no electrical resistance to dc currents, no heating or losses of any sort and therefore a current produced in a superconducting ring will persist forever. Additionally, a superconductor expels applied magnetic fields such that the magnetic field is zero everywhere inside. Although classical physics cannot explain the superconductivity phenomenon, the superconducting state is a special quantum condensation of electrons as verified through observations such as the quantitation of magnetic flux produced by a superconducting ring [Ref. 23]. Keeping these properties in mind, it doesn't take much thought in coming up with just a few of the endless possible applications of the phenomenon called superconductivity.

Superconductivity was discovered in 1911 by the Dutch physicist Heike Kamerlingh Onnes when he was studying pure mercury at very low temperatures and observed an unmeasurable small value of resistance at 4.15 Kelvin (K). The

definition therefore, of a superconductor, in which the resistivity is zero when the temperature is lowered below a certain characteristic temperature called the critical temperature (T_c), is a perfect conductor. These materials lose their superconductivity properties, however, above a certain temperature dependent critical magnetic field $\{B_c(T)\}$. Superconductors are grouped into two types. Type I being pure elements which are characterized by one temperature dependent critical magnetic field and Type II being those which are characterized by two and are typically compounds.

The theory of superconductivity can be best presented by explaining Type I superconductors. As stated earlier, Type I superconductors are those elements which are characterized by one critical magnetic field. It is found that the Type I critical magnetic field varies with temperature according to the relation:

$$B_c(T) = B_c(0) \left[1 - \left(\frac{T}{T_c} \right)^2 \right] \quad (C-1)$$

where, from this equation it is evident that $B_c(T)$ exhibits a maximum at $T = 0$ K [Ref. 23]. From Amperes-Maxwell's Law, the maximum current therefore, that can be sustained in a Type I superconductor is limited by the value of the $B_c(T)$. Additionally, if an applied magnetic field exceeds $B_c(0)$ the element will never become superconducting at any temperature, and because of the inherent low

values of the critical field characteristics of Type I superconductors, this group is not used for the construction of superconducting magnets, or high field magnets.

In addition to the property of zero resistance, another condition which must be satisfied for a material to be a superconductor is that the material must demonstrate the Meissner effect. The Meissner effect is the expulsion of magnetic fields from the interior of a superconductor such that $B = 0$ and is the phenomenon that explains magnetic levitation. From Ohm's Law, if the resistivity of a superconductor is zero so is the electric field in its interior and therefore, from Faraday's Law of induction, the magnetic flux in a superconductor cannot change. Hence, the magnetic field is constant in a superconductor. In fact, in 1933 Meissner discovered that when a metal becomes superconducting, the magnetic field is expelled so that $B = 0$ everywhere inside a superconductor. Therefore, in addition to being a perfect conductor, a superconductor is also a perfect diamagnet; and due to this last condition, a superconductor will repel a permanent magnet and therefore levitate.

The expulsion of magnetic field in the interior of a superconductor actually stems from the induction of surface currents which create an equal and opposite magnetic field. These currents penetrate the superconductor to a depth called the penetration depth and varies according to the relation:

$$\lambda(T) = \lambda_0 \left[1 - \left(\frac{T}{T_c} \right)^4 \right]^{-\frac{1}{2}} \quad (C-2)$$

where λ_0 is the penetration depth at $T = 0$ K [Ref. 23]. This implies that as T approaches T_c , the applied magnetic field penetrates deeper into the superconductor until the entire sample is penetrated and the material returns to its normal state. The penetration depth is of great importance when dealing with thin film superconductors as can be imagined.

In contrast to thin film samples, bulk samples develop a magnetization, M , when subjected to an external magnetic field which is related to the magnetic field by:

$$B_{\text{internal}} = B_{\text{external}} + \mu_0 M \quad (\text{C-3})$$

Since $B_{\text{internal}} = 0$ for a superconductor, equation (29) reduces to:

$$M = -\frac{B}{\mu_0} = \chi B \quad (\text{C-4})$$

where $\chi = -1/\mu_0$ and is called the magnetic susceptibility [Ref. 23]. This states that the magnetization opposes the external magnetic field which again supports the essential fact that a superconductor exhibits perfect diamagnetism.

The critical magnetic field can also be described in terms of the energy increase of the superconducting state due to the exclusion of magnetic flux from its interior compared to the normal state, which allows the flux to penetrate, and is given by the expression:

$$E_s + \frac{B_c^2}{2\mu_0} = E_n \quad (C-5)$$

where E_s is the energy of the superconducting state, E_n is the energy of the normal state and $B_c^2/2\mu_0$ is the energy increase [Ref. 23]. Although simple electricity and magnetism can explain most of Type I and Type II phenomena, type II superconductors are generally more complex.

Type II superconductors are characterized by two critical magnetic fields. Below B_c (lower) they behave like a Type I superconductor and above B_c (upper) the superconductor returns to its normal state. When the magnetic field is between these two boundaries, the superconductor is in a mixed state and any current that is present may lead to a motion of vortices perpendicular to the direction of the current and therefore; the mixed state is often thought of as a vortex state [Ref. 23]. If the current is large enough, these vortices will increase the resistance above zero and return the superconductor to its normal state. The value of that current which produces vortices sufficiently large enough to destroy the superconducting state is called the critical current (J_c). Defects created in a superconductor, such as those created with high energy electron irradiation, provide pinning centers for the vortices, or changes in flux with time. Therefore, as a current flows through the superconductor the pinning sites trap the vortices

and result in zero resistance in the mixed state, and thereby, increase the critical current.

In comparison to Type I superconductors, those amongst Type II have much larger critical magnetic fields and are therefore the superconductors utilized for practical applications. One possible application is the exploitation of the supercurrents which are associated with large magnetic fields. For instance, if a superconducting ring with $T < T_c$ is placed in an external magnetic field, the magnetic flux will pass through the hole in the loop despite not penetrating the interior of the superconductor. When the external field is removed, the flux through the hole in the loop will remain trapped, because the flux through a superconductor cannot change, and therefore; an induced current will appear in the loop. If the dc resistance in the loop is zero, the current will persist forever.

In addition to their electromagnetic properties, superconductors have equally unique thermal properties which help in understanding the theory behind superconductivity. When heat is added to a metal, the energy is used to excite lattice vibrations and to increase the kinetic energy of the conduction electrons. The electronic specific heat, C , of a metal is defined as the ratio of the heat absorbed by the electrons to the corresponding temperature increase. For a normal metal at low temperatures, the specific heat varies according to the relation:

$$C = AT + BT^3 \quad (C-6)$$

where the linear term is due to electronic excitations and the cubic term is due to the lattice vibrations [Ref. 23]. In contrast, however, the specific heat of a superconductor suffers a large increase at T_c resulting in a discontinuity and thereafter decreases by $\exp(-E_g/2kT)$, where E_g is the energy gap and can be explained by the BCS theory of superconductivity.

The BCS theory, named for Bardeen, Cooper and Schrieffer is the accepted theory for explaining the superconducting state. As electrons travel near lattice ions, the coulomb interaction displaces the ions such that a local positive charge density is produced. As more electrons pass the displaced ion, it oscillates at the speed of sound and behaves as a harmonic oscillator. The quantum of this lattice vibration is a phonon, and as each of the phonons travel through the lattice, they act as an attractive force as they encounter other electrons. This electron-phonon-electron interaction couples two electrons which are called a Cooper pair and is the central theme of the BCS theory. As the coupled electrons have equal and opposite spin and momenta; a Cooper pair forms a system with zero total momenta and spin, and therefore act as bosons and may all be in the same state.

The attractive force between the electrons is not strong enough however to overcome their coulomb repulsion and therefore they are separated by a distance known as the coherence length. One author describes the Cooper pair as

analogous to a helium atom in that both are bosons and have zero spin; and just as the super fluidity of liquid helium is viewed as a condensation of bosons in the ground state, superconductivity may be viewed as a super fluid state of Cooper pairs, all in the same quantum state [Ref. 23]. According to the BCS theory, a ground state is defined as the state in which all electrons form Cooper pairs which in turn are all in the same quantum state of zero momenta. Because the phonons emitted by a Cooper pair interact with other pairs, all pairs act collectively and it becomes impossible to differentiate one pair from the other in terms of their momentum. Therefore lattice imperfections and vibrations, which scatter electrons in normal metals, have no effect on Cooper pairs and therefore the resistivity is zero. Additionally, if no magnetic field is present, all pairs have zero momentum and; conversely; if a magnetic field is applied all pairs will have the same momentum. If the magnetic field is large enough, the Cooper pairs will break up into a state where both spins are pointing in the same direction as to lower their energy. This is the upper value of the critical magnetic field and explains the magnetic field breakdown of a superconductor.

Due to these "collective" properties, a condensed state of Cooper pairs can be represented by a single coherent wave function, and the stability of the superconducting state, therefore, is heavily dependent upon the correlation between Cooper pairs. This behavior can be explained in terms of the energy levels of a superconductor. The attraction of Cooper pairs lowers the energy of

the pair relative to the Fermi energy of the unpaired electrons due to the work necessary in separating the electrons. This difference in energy is called the energy gap, E_g , and it represents the energy required to break up a Cooper pair. This energy gap exists between the ground state and excited state of superconductor only. Recall that for a normal conductor at $T = 0\text{ K}$; all states below the Fermi energy, the largest kinetic energy free electrons can have at $T = 0\text{ K}$, are filled and likewise all states above the Fermi energy are empty. Although, the energy gap for a superconductor is small as compared to a semiconductor, the gap is large enough to cause differences in specific heats for superconductors and normal metals; and varies according to the relation:

$$E_g = 3.53 \kappa T_c \quad (\text{C-7})$$

whereupon it is evident that superconductors with large energy gaps have higher critical temperatures [Ref. 23]. Additionally, as the temperature increases, thermally excited electrons interfere with Cooper pairs and reduce the energy gap until it reaches zero at the critical temperature.

The continued research on superconductors paid off in 1987 when high temperature superconductors were developed so that liquid nitrogen vice helium can be used to develop the superconducting state. The first high temperature superconductor was the Y123 compound developed at the University of Houston. The Y123 superconductor has a fully ordered crystal lattice consisting of planes

of yttrium, barium and copper, in which none of the metals mix. In between the yttrium and barium layers, copper atoms combine with oxygen atoms in pyramids. The pyramid bases face each other across the yttrium plane and form the ab plane which is the supercurrent carrying plane. The c-axis is perpendicular to this plane and is the axis which angular irradiation is referenced. In between the two consecutive layers of barium, copper and oxygen again combine in a flat diamond, the corners of which are connected to other similar diamonds. Figure C1 is an illustration of the Y123 crystalline structure [Ref. 24]. It is apparent from the crystalline structure; therefore, that the properties of Y123 and other similar high temperature superconductors are heavily dependent upon the peculiar bonding between the copper and oxygen atoms. In 123 compounds, the oxygen content changes the copper's valence state and a resulting strong correspondence with superconducting properties exist [Ref. 24], and as stated earlier, a material with too many oxygen vacancies will not superconduct. Additionally, because different isotopes of oxygen, barium and copper do not alter the 123 superconductor properties at all; whereas other superconductors change with different isotopes, the phonon interaction, heavily dependent on mass may not be the major contributor to electron pairing in ceramic superconductors [Ref. 24]. Two possible explanations are that excitons (electron hole pairs) provide attraction and the other theorizes that magnetic interactions provide attraction for the electron pairs [Ref. 24]. To date, there is no one accepted theory for electron interaction in

high temperature superconductors but continued research into their properties will, no doubt, develop one soon.

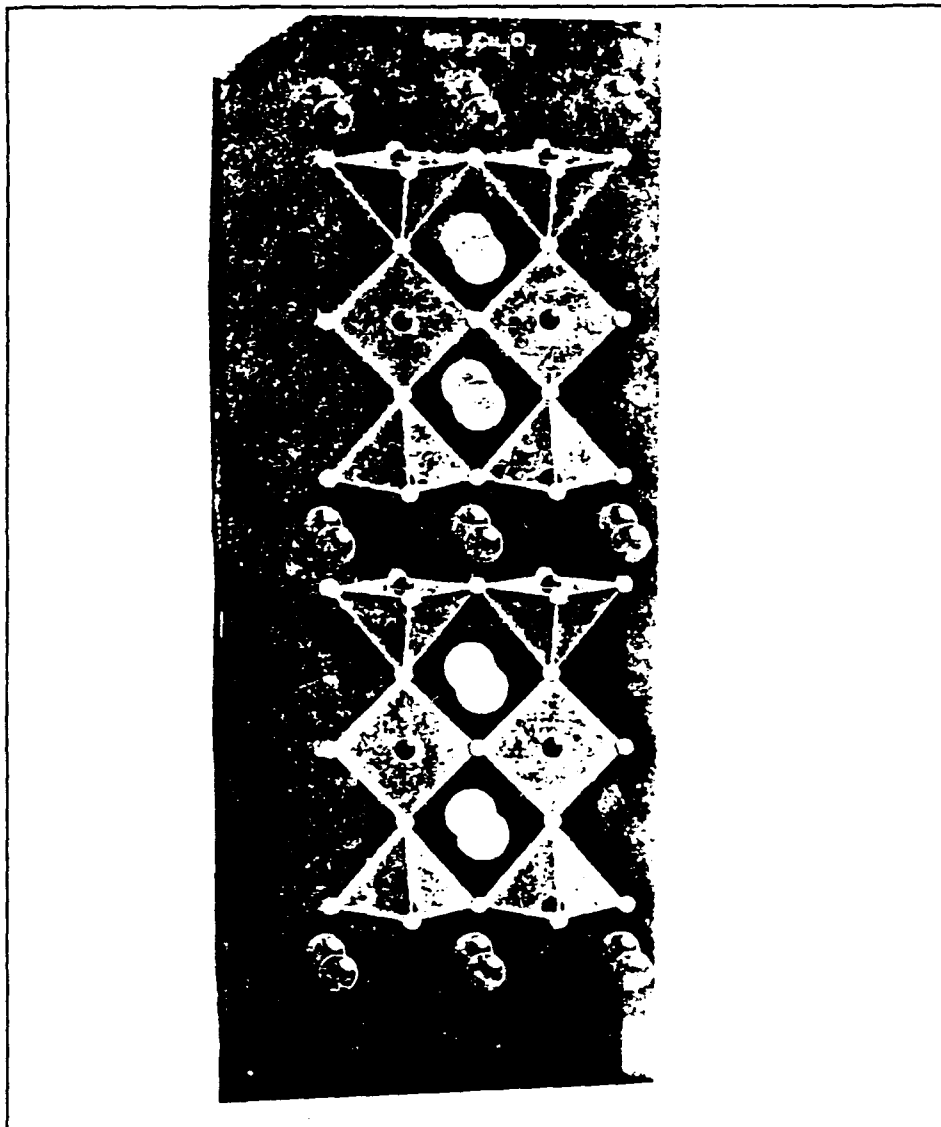


Figure C1. Y123 Crystalline Structure.
The large black balls represent Yttrium, the large white balls represent Barium, the small black balls represent Copper and the small white balls represent Oxygen. [Ref. 24]



**Texas Center for Superconductivity
at the University of Houston
Houston, Texas 77204-5932**

**Defect Size Dependence of Critical Current Density Enhancement for Irradiated
 $YBa_2Cu_3O_{7.8}$**

**J. Bechtold, Y. Y. Xue, Z. J. Huang, E. V. Hungerford, P. H. Hor, C. W. Chu, X. K.
Maruyama, H. Backe, F. R. Buskirk, S. M. Connors, D. D. Snyder, Y. C. Jean and J. W.
Farmer**

Submitted to *Applied Physics Letters*, June 7, 1991

Abstract

The effects of electron and fast neutron irradiation on the superconducting properties of melt-textured $YBa_2Cu_3O_{7.8}$ is studied experimentally. By comparing the critical current density enhancement effects normalized to the total atomic displacement damage, it is found that the enhancement depends heavily on the type and energy of radiation and on the beam direction with respect to the crystal. A model based on defect size is proposed to interpret the effects. The results show that defects of $\sim 30 \text{ \AA}$ are at least 10^3 times more effective than point defects.

Supported by:

NSF Low Temperature Physics Program Grant DMR 86-126539, DARPA Grant MDA 972-88-G-002, NASA Grant NAGW-977, Texas Center for Superconductivity at the University of Houston, T. L. L. Temple Foundation, MURR Grant DE-FG02-90ER45427, NSWC, Naval Postgraduate School, State of Texas

Limited Distribution Notice:

This preprint is intended for publication in a journal or proceeding and changes may be made before publication. It is issued for early dissemination of its contents and may be cited or reproduced only with the permission of the authors.

PHONE: (713) 743-8200 FAX: (713) 743-8201

Defect size dependence of critical current density enhancement for
irradiated $\text{YBa}_2\text{Cu}_3\text{O}_{7-\delta}$

J. Bechtold, Y. Y. Xue, Z. J. Huang, E. V. Hungerford, P. H. Hor and C. W. Chu
Department of Physics and Texas Center for Superconductivity at the
University of Houston, Houston TX 77204-5932

X. K. Maruyama, H. Backe,* F. R. Buskirk, S. M. Connors and D. D. Snyder
Department of Physics, Naval Postgraduate School, Monterey CA 93943

Y. C. Jean
Department of Chemistry, University of Missouri, Kansas City MO 64110

J. W. Farmer
Research Reactor, University of Missouri at Columbia, Columbia MO 65211

The effects of electron and fast neutron irradiation on the superconducting properties of melt-textured $\text{YBa}_2\text{Cu}_3\text{O}_{7-\delta}$ is studied experimentally. By comparing the critical current density enhancement effects normalized to the total atomic displacement damage, it is found that the enhancement depends heavily on the type and energy of radiation and on the beam direction with respect to the crystal. A model based on defect size is proposed to interpret the effects. The results show that defects of $\sim 30 \text{ \AA}$ are at least 10^3 times more effective than point defects.

* permanent address: Institut für Physik der Universität, Postfach 3980, D-65 Mainz 1, Germany.

Date of Submission: June 7, 1991
Journal of Submission: Applied Physics Letters
Key Words: irradiation, defect size, high temperature superconductor,
critical current density, Y123
PACS: 74.60.Ge, 74.60.Jg, 61.80.Fe, 61.80.Hg

I. INTRODUCTION

One of the critical frontiers for practical use of high temperature superconductors (HTS's) is the effective introduction of artificial pinning centers to increase the current carrying capacity. Based on the pinning models and the measured coherence lengths (ξ) of HTS's, defects of 30 to 100 Å have been commonly accepted as effective pinning centers. However, it has been suggested that much smaller and larger defects may also play an important role in enhancing J_c , although efforts made to introduce such defects have not been entirely successful. Civale *et al.*¹ proposed that point defects were responsible for the large J_c enhancement of their proton-irradiated $\text{YBa}_2\text{Cu}_3\text{O}_{7-\delta}$ (Y123) single crystal. Along this line, various cation substitutions might also be expected to be beneficial. On the other hand, M. Murakami *et al.*² suggested that large Y_2BaCuO_5 (Y211) precipitates ($\sim \mu\text{m}$ size) are pinning centers in melt-textured Y123. Tiny segregated second-phase particles introduced by nonstoichiometric composition would then be a good candidate for J_c enhancement. With the existence of such disparate views on the size of an effective pinning center, it is clear that knowledge of the size- and shape-dependence of the pinning force is very important.

Using fast neutron and electron irradiation of various energies we have produced defects with sizes ranging from point displacements to extensive amorphous tracks ($\sim \mu\text{m}$). Although irradiation by electrons³⁻⁵ and fast neutrons⁶⁻⁸ has been previously performed, we present for the first time a systematic comparative study of their effects on J_c . By adopting the change in critical temperature (T_c) as the measure of the atomic displacement damage, we are able to determine quantitatively the

relative effectiveness of the various beams and energies. In this way, it is found that fast neutron irradiation is the most effective in enhancing J_c . From comparison of the beam effectiveness the importance of defect size in flux pinning is induced. Preliminary results show that defects of 10 to 20 Å and above are required for substantial increases in J_c . However, much larger track-like defects $\leq 1 \mu\text{m}$ are counter-productive when perpendicularly oriented to the field, placing an upper-limit on the defect size.

II. EXPERIMENTAL

Samples of melt-textured Y123 ($\sim 1.1 \times 1.1 \times 0.7 \text{ mm}^3$), whose preparation is described in Ref. 9, were dry cut with a diamond wafer blade. The material was well oriented with the c-axis parallel to within 3 degrees of the shortest dimension as verified by XRD. The electron irradiation was carried out at the Naval Postgraduate School Linac in flowing oxygen under ambient conditions with an average current of 0.3 to 0.7 μA in a 3.5 mm beam diameter. The maximum fluence obtained was $(3.6 \pm 0.6) \times 10^{18} \text{ e/cm}^2$. Four sets of samples were irradiated with the corresponding angle between the c-axis and the electron beam being 0°, 30°, 60°, and 90°. Fast neutron irradiation was done at the University of Missouri Research Reactor to a maximum fluence of $4 \times 10^{18} \text{ n/cm}^2$. All samples were measured with a VSM or SQUID magnetometer before and after the irradiation. The preirradiation values of J_c (77 K, 1 T) were greater than 10^4 A/cm^2 for all samples studied.

III. DISCUSSION

The central point of this work is to compare the effects of different types of irradiation and thus the effects of different defect sizes on the flux pinning force. For that purpose, proper measurement of the total radiation damage is critical. Of the two types of radiation damage, ionizing and nonionizing, it has been shown that ionization energy loss is not important to superconductivity. Summers *et al.*¹⁰ show that the decrease in T_c (ΔT_c) of Y123 is linearly proportional to the nonionizing energy loss for many different particles and energies. They further proposed that the nonionizing energy loss is proportional to the total atomic displacement density, regardless of whether the atomic displacements are grouped in clusters or are in the form of isolated point defects. ΔT_c is therefore a measurement of the total nonionizing radiation damage, or equivalently, the total number of atomic displacements. The value of ΔT_c may be measured experimentally or calculated based on the dose and the nonionizing energy loss of the beam. In the case of 100 MeV electrons, for example, it was possible to do both. Our measured T_c loss of $0.8 \text{ Kcm}^2/10^{18} \text{ e}$ is in reasonable agreement with Summers' prediction of $1.0 \text{ Kcm}^2/10^{18} \text{ e}$.

The increase in J_c for 100 MeV electron and fast neutron irradiation is plotted in Fig. 1 using ΔT_c as the dosage parameter. From the figure it can be seen that the fast neutron irradiation results in a greater increase in J_c . Another feature observable in Fig. 1 is the semilinear increase of J_c for the fast neutron irradiation followed by a saturation. This feature has also been observed in other studies such as 3 MeV proton,¹ 3 MeV electron,⁵ fast neutron,⁸ and 2 MeV proton¹³ irradiation. While there is insufficient

data to make this conclusion for the 100 MeV electron irradiation, it is reasonable to conclude that a similar behavior exists. In the case of the individual pinning model a linear dependence of J_c on dose is expected. However, the prediction of linear behavior is not restricted to individual pinning. In the $2D^{11}$ and the $1D^{12}$ collective pinning theories, a semilinear dose dependence of J_c is also predicted.

Our goal in comparing the effectiveness of different irradiations is simplified by the presence of the nearly linear increase in J_c . To compare the beam effectiveness on an equal footing we calculate $\Delta J_c B / \Delta T_c$ in the linear region. This amounts to normalizing the increase in pinning force to the total atomic displacement damage. Values of $\Delta J_c B / \Delta T_c$ at 77 K and 1 T are shown in Table I for our electron and fast neutron irradiation. Also included in Table I are values of $\Delta J_c B / \Delta T_c$ calculated from Refs. 1, 4, 6-8, and 13 for various irradiations of single crystal and quasi-single crystalline Y123. Due to the normalization, differences in $\Delta J_c B / \Delta T_c$ among different irradiation techniques are caused solely by the distribution (not the amount) of the induced damage. In fast neutron damage, for example, nearly all atomic displacements occur in cascades of energy $1 \text{ keV} < E < 200 \text{ keV}$.¹⁴ These cascades generate clusters of atomic displacements which may be interpreted as large defects. On the other hand, electrons and low energy protons which interact mainly through the long range weak Coulomb potential, predominantly produce isolated point defects. The greater effectiveness of fast-neutron irradiation is likely due to the presence of these larger size defects.

An independent test of defect-size effects was made by irradiating with 100 MeV electrons at four different angles to the c-axis. As mentioned previously, the main defects created here are point defects, which are small enough that they should behave isotropically to the field. Only the collisions with energy transfer $> 10^5$ eV are expected to produce extensive cylindrical defects which could behave anisotropically to the field. Compared to the point defects, these large defects are at the ppm level. Since angular dependence is observed, as shown in Fig. 2, these rare defects must play a disproportional role either as pinning centers when the field is parallel to the defects or as weak links when the field is perpendicular to them. The similar anisotropic behavior is observed at various doses, so the percolation between these extensive defects could not be the only reason for anisotropy.

In order to obtain a more quantitative picture of the importance of defect size in flux pinning we consider the average primary knock-on recoil energy $\overline{E_p}$ produced by different types of radiation. Cascades of total energy E_p are initiated by the primary knock-on atom. The size of cluster defect generated in these cascades is an increasing function of E_p . Due to the Coulomb interaction, electrons and low energy protons have¹⁵ $\overline{E_p} \equiv E_d \ln(E_p(\text{max})/E_d)$ where E_d is the minimum energy to create one displacement. For the electron and proton irradiation considered here, $\overline{E_p}$ averaged over collisions with Y, Ba, Cu, and O is on the order of 10^2 eV. Fast neutrons, interacting through a nearly hard-sphere potential have $\overline{E_p} = E_p(\text{max})/2$. The value of $\overline{E_p}$ is about 10^4 eV averaged over all collisions in Y123. A plot of the normalized flux pinning force enhancement vs $\overline{E_p}$ is shown in Fig. 3. Although there is a significant spread in the values, it is

apparent that the enhancement is higher for higher $\overline{E_p}$. The steep rise in force from 3 MeV to 100 MeV electron irradiation is indicative of a threshold. The threshold appears to be at 200 eV recoil energy from the graph but is probably at higher energy due to the tail in the distribution of E_p 's above $\overline{E_p}$. The lower rate of increase in force from 100 MeV electron to fast neutrons indicates a saturation in the total normalized pinning force with defect size.

The data above is taken as evidence of far greater flux pinning enhancement for defects larger than point defects. Nevertheless, the high ratio of point defects to cluster defects in 3 MeV proton irradiation¹ and the absence of visible defects $> 15 \text{ \AA}$ in TEM images from 1 MeV electron irradiated Y123 has been offered¹⁶ as evidence for point defect pinning. In attempt to resolve this controversy we consider the defect density in a typical cascade initiated by a 1 keV oxygen recoil. The number of defects (including vacancies, interstitials, and replacements) created in a cascade of energy E_p is E_p/E_d . Using $E_d = 20 \text{ eV}$ the number of defects created is about 50. The projected range of a 1 keV oxygen recoil in Y123 was estimated at 30 \AA from a Monte Carlo simulation.¹⁷ If the volume of the defect is taken as $4\pi/3 (15 \text{ \AA})^3$ the local defect density will be 0.050 dpa. According to Summers *et al.* this defect density amounts to a local T_c depression of $\approx 30 \text{ K}$, which is sufficient for the region to act as a pinning center. Numerical simulation, however, of similar defects has shown that this type of defect may not be visible by TEM.¹⁸

The existence of a defect-size window for effective flux pinning is consistent with other experimental observations. The lack of significant

enhancement of J_c in chemical substitution experiments supports the conclusion that point-like defects are not effective.¹⁹ Furthermore, the angular data shows that when the defect is too large in the direction of vortex motion it can act as a weak link. This implies that large scale chemical impurities such as Y211 precipitates may not be viable flux pins. Finally, fast neutron irradiation is expected to be far superior to charged particle irradiation for increasing transport J_c since the percentage of point defects is much lower. This seems to be the case based on fast neutron,²⁰ proton,²¹ and electron²² irradiation of thin films, as well as our bulk electron and fast neutron irradiation.

In summary, it has been observed that enhancement of J_c strongly depends on the type and energy of radiation and on the beam direction. The dependence of the normalized pinning force enhancement on the average primary knock-on energy indicates a threshold defect-size for effective flux pinning exists. The lower range for effective pinning is a cascade defect 10 to 20 Å in size. Defects of this size and larger are at least 10^3 times more effective in flux pinning than point effects.

IV. ACKNOWLEDGEMENT

We would like to acknowledge Dr. R. L. Meng for the preparation of the melt-textured Y123 and Drs. H. W. Zandbergen, J. Kulik, K. B. Ma, and W. K. Chu for beneficial discussions.

This work is supported in part by the NSF Low Temperature Physics Program Grant No. DMR 86-126539, DARPA Grant No. MDA 972-88-G-002, NASA Grant No. NAGW-977, Texas Center for Superconductivity at the

University of Houston, and the T. L. L. Temple Foundation. One of the authors, J. W. Farmer, would like to acknowledge MURR support through grant number DE-FG02-90ER45427. The work at NPS is sponsored by the NSWC and the Naval Postgraduate School.

TABLE I.

Values of the normalized J_c enhancement and the average primary recoil energy for various beams and energies are shown for this work and other studies on high quality Y123.

Source	Reference	$\Delta J_c B / \Delta T_c$ (AT/Kcm ²)	$\overline{E_p}$ (eV)
(77 K, 1 Tesla)			
3 MeV e ⁻	[4]	1.8×10^3	6.8×10^1
3 MeV p	[1]	1.5×10^4	2.0×10^2
3.5 MeV p	[13]	1.0×10^5	3.0×10^2
100 MeV e ⁻	this work	$4.0 \times 10^4 - 1 \times 10^5$	2.1×10^2
fast neutron	[6]	5.6×10^6	2.0×10^4
fast neutron	[7]	2.0×10^5	2.0×10^4
fast neutron	[8]	9.0×10^4	2.0×10^4
fast neutron	this work	6.0×10^5	2.0×10^4

REFERENCES

01. L. Civale, A. D. Marwick, M. W. McElfresh, T. K. Worthington, A. P. Malozemoff, F. H. Holtzberg, J. R. Thompson, M. A. Kirk, *Phys. Rev. Lett.* 65, 1164 (1990).
02. M. Murakami, *Mod. Phys. Lett. B* 4, 163 (1990).
03. F. R. Buskirk, J. R. Neighbours, X. K. Maruyama, E. L. Sweigard, L. J. Dries, C. Y. Huang, F. A. Junga, *IEEE Trans. Nucl. Sci.* 35, 1487 (1988).
04. T. Kato, K. Shiraishi, J. Kuniya, *Jpn. J. Appl. Phys.* 28, L766 (1989).
05. K. Shiraishi, T. Kato, J. Kuniya, *Jpn. J. Appl. Phys.* 28, L807 (1989).
06. R. B. Van Dover, E. M. Gyorgy, L. F. Schneemeyer, J. W. Mitchell, K. V. Rao, R. Puzniak, *Nature* 342, 55 (1989).
07. H. Küpfer, U. Wiech, I. Apfelstedt, R. Flükiger, R. Meier-Hirmer, T. Wolf, H. Scheurer, *IEEE Trans. Magn.* 25, 2303 (1989).
08. F. M. Sauerzopf, H. P. Wiesinger, W. Kritscha, H. W. Weber, G. W. Crabtree, J. Z. Liu, *Phys. Rev. B* 43, 3091 (1991).
09. L. Gao, R. L. Meng, Y. Y. Xue, P. H. Hor, and C. W. Chu, *Appl. Phys. Lett.* 58, 1 (1991).
10. G. P. Summers, E. A. Burke, D. B. Chrissey, M. Nastasi, J. R. Tesmer, *Appl. Phys. Lett.* 55, 1469 (1989).
11. Z. D. Wang, Z. J. Huang, Y. Y. Xue, P. H. Hor, C. S. Ting, C. W. Chu, submitted to *Phys. Rev. B*.
12. T. K. Worthington, *APS Bulletin* 36, 336 (1991). In the case of 1-D collective pinning the dose dependence is only semilinear but probably cannot be ruled out from the experimental observations.
13. R. B. van Dover, E. M. Gyorgy, A. E. White, L. F. Schneemeyer, R. J. Felder, J. V. Waszczak, *Appl. Phys. Lett.* 56, 2681 (1990).

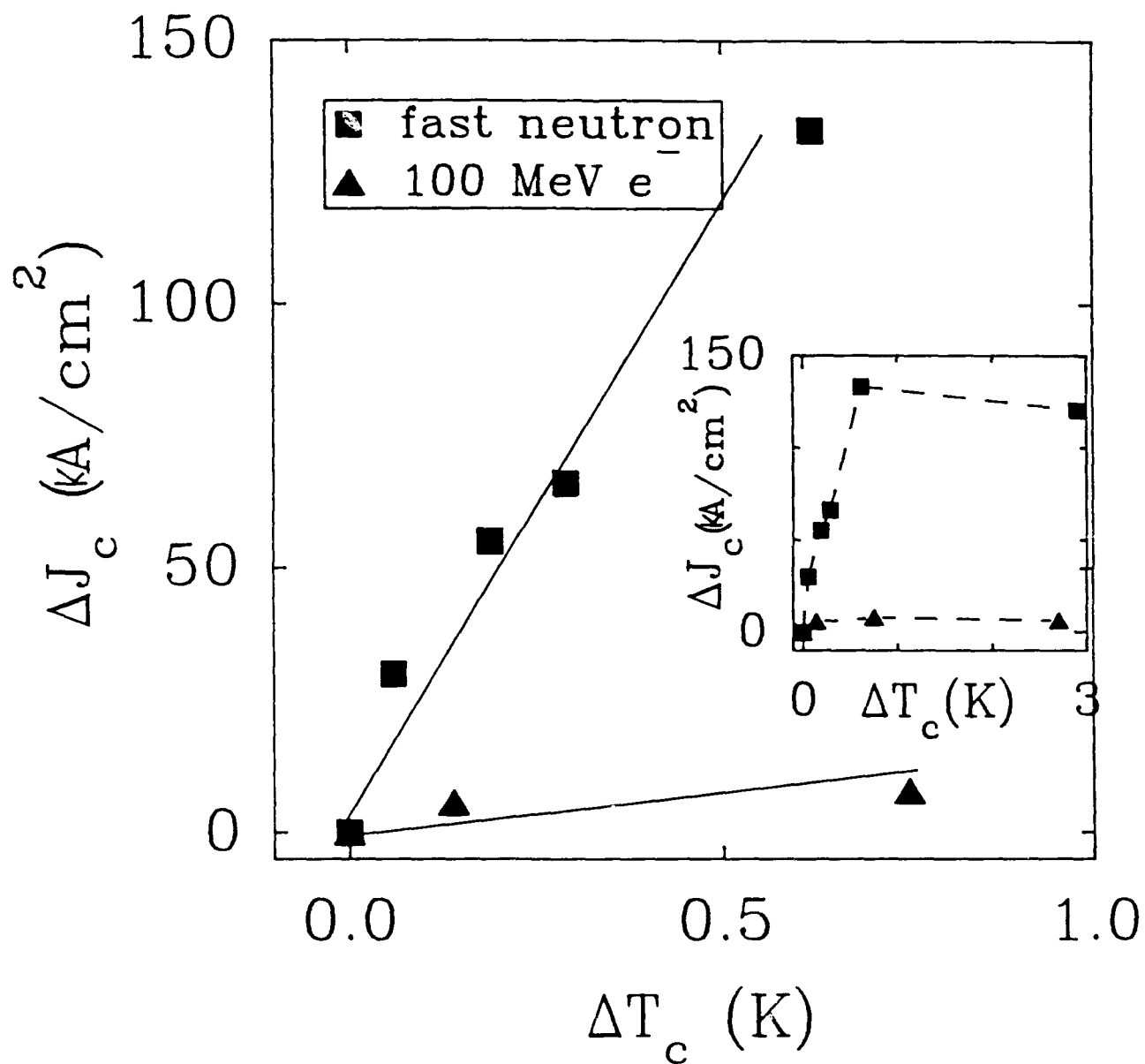
14. C. A. English, M. L. Jenkins, "Heavy-Ion Damage in Solids," in *Treatise on Heavy-Ion Science*, ed. D. A. Bromley (New York: Plenum Press, 1985), p. 327.
15. D. Billington and J. Crawford, *Radiation Damage in Solids*, (Princeton: Princeton University, 1961), p. 22.
16. M. A. Kirk, APS Bulletin 36, 833 (1991).
17. K. B. Ma, private communication.
18. H. W. Zandbergen, J. Kulik, B. Nieuwendijk, submitted to Physica C, March 20, 1991.
19. S. Jin, T. H. Tiefel, G. W. Kammlott, R. A. Fastnacht and J. E. Graebner, Physica C 173, 75 (1991).
20. W. Schindler, B. Roas, G. Saemann-Ischenko, L. Schultz, and H. Gerstenberg, Physica C 169, 117 (1990).
21. R. Soulen, D. B. Chrisey, J. H. Horwitz, B. D. Weaver, M. E. Reeves, D. A. Krieger, DARPA 2nd Annual HTSC Workshop, October 3-5, 1990.
22. T. Terai, T. Masegi, Y. Takahashi, Y. Enomoto and S. Kuro, Jpn. J. Appl. Phys. 29, L2053 (1990).

FIGURE CAPTIONS

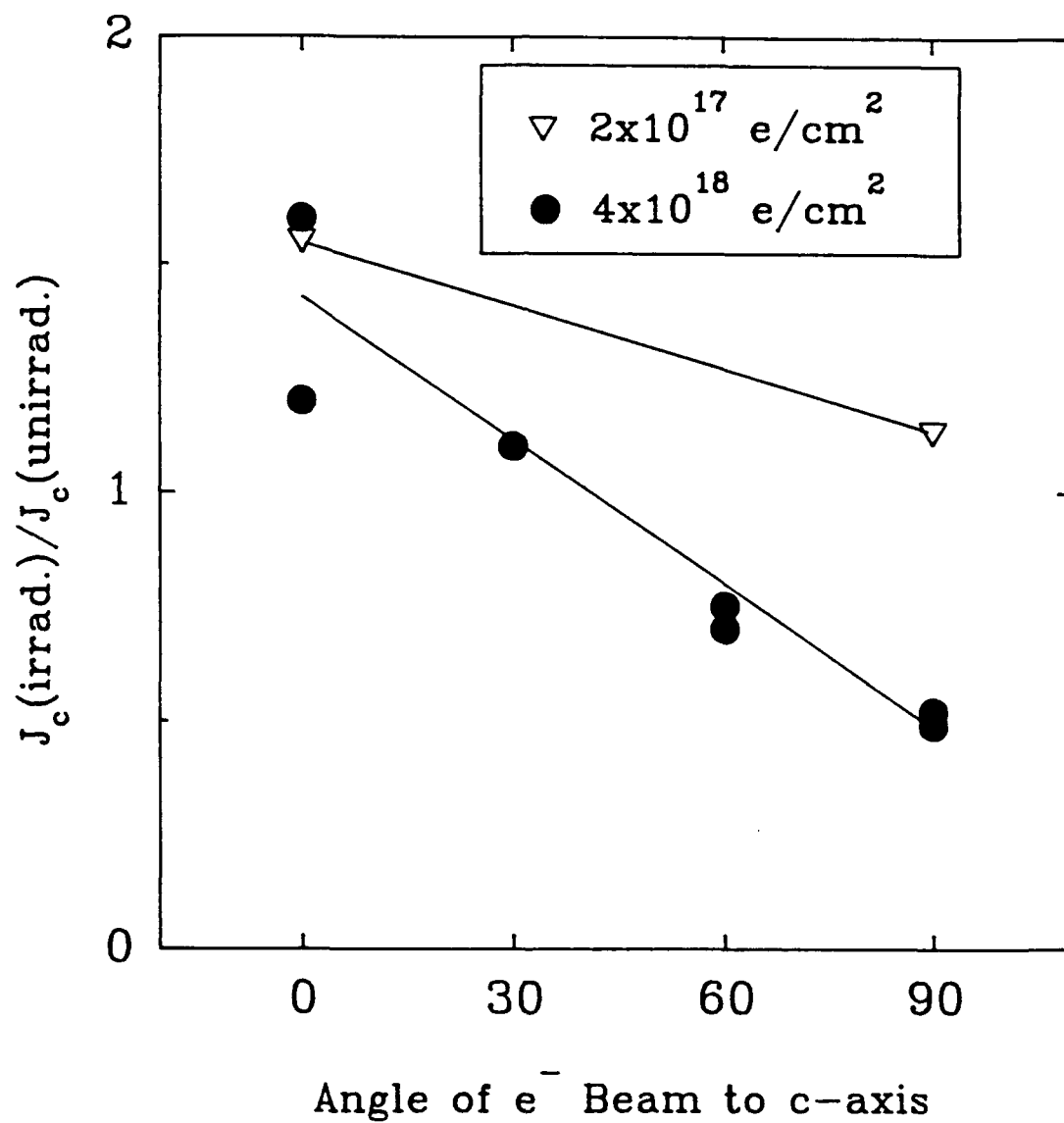
Figure 1. Increase in J_c for fast neutron and 100 MeV electron irradiation at 77 K and 1 T compared using the atomic displacement damage parameter ΔT_c .

Figure 2. The dependence of J_c enhancement on the angle of 100 MeV electrons to the c-axis of Y123 at two doses 2×10^{17} e/cm² and 4×10^{18} e/cm².

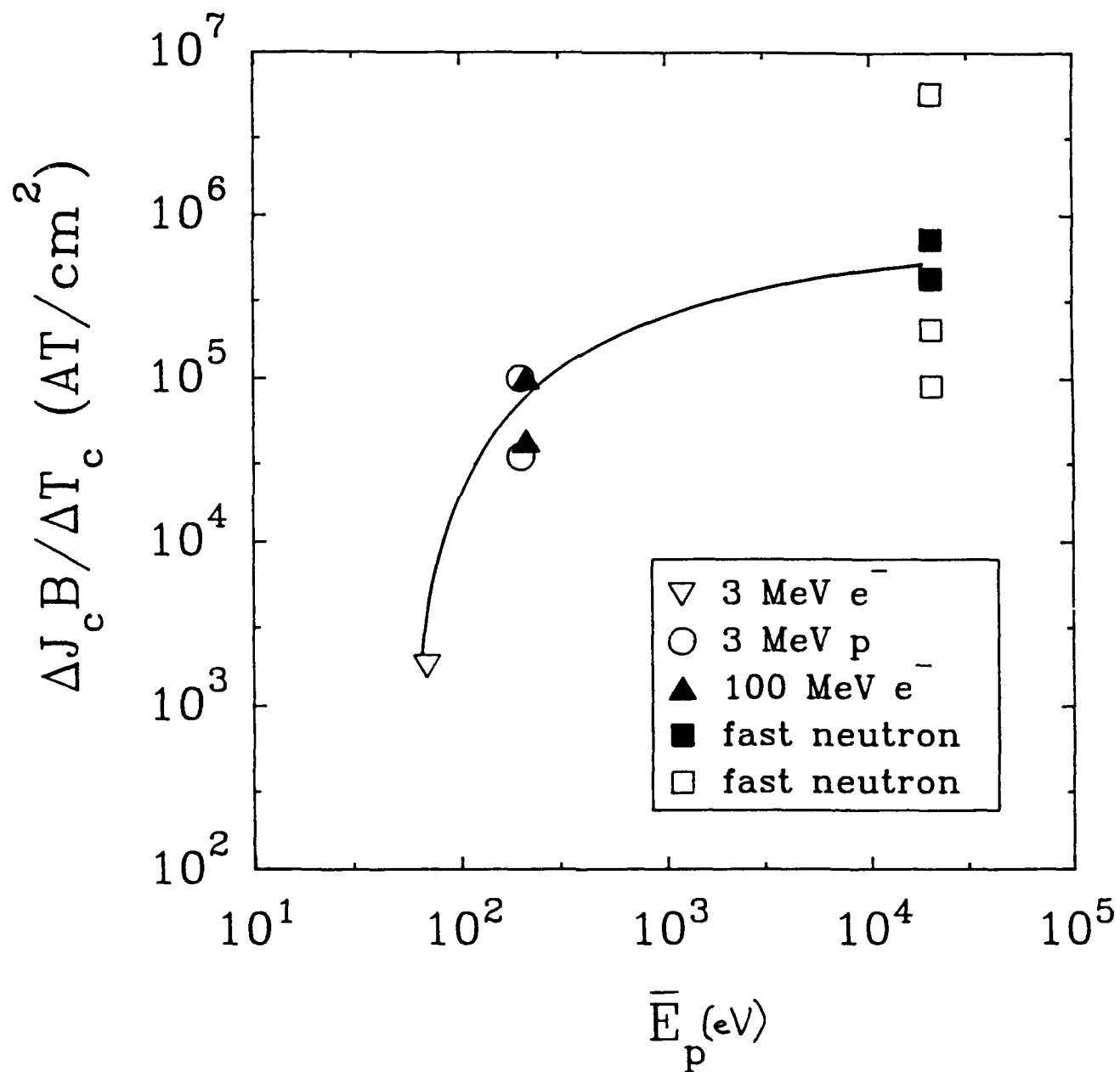
Figure 3. Plot showing the relationship of the enhancement per unit damage $\Delta J_c B / \Delta T_c$ at 77 K and 1 T, to the average primary knock-on energy $\overline{E_p}$. Bold data points are from this work. Other data is drawn from Refs. 1, 4, 6-8, and 13, and are identified in Table I.



Bechtol
et al.
Fig. 1



Bechtold
et al.
Fig. 2



Bechtol
et al.
Fig. :

LIST OF REFERENCES

1. Sweigard, E.L., *Effects of 67.5 MeV Electron Irradiation on Y-Ba-Cu-O and Gd-Ba-Cu-O High-Temperature Superconductors*, Master's Thesis, Naval Postgraduate School, Monterey, California, December 1987.
2. Wolfe, G.J., *Effects of Large Doses of High Energy Electrons on a $\text{YBa}_2\text{Cu}_3\text{O}_{7.8}$ High Temperature Superconductor*, Master's Thesis, Naval Postgraduate School, Monterey, California, December 1989.
3. Hammerer, John J., *Effects of Neutron Irradiation on High Temperature Superconductors*, Master's Thesis, Naval Postgraduate School, Monterey, California, June 1988.
4. Meyer, O., *Ion Beam Modification and Analysis of Thin YBa Cu O Films*, Kernforschungszentrum Karlsruhe, Institut for Nuklear Festkorperphysik, Karlsruhe, FRG, 1989.
5. Konezykowski, M. et al., *Physica C*, Vol. 162-164, pp. 747-748, 1989.
6. Kupfer, H. et al., *Cryogenics*, Vol 29, pp. 268-279, 1989.
7. van Dover, R. B. et al., *Nature*, Vol. 342, pp. 55-57, 1989.
8. Kato, T. et al., *Japanese Journal of Applied Physics*, Vol. 28, No. 5, pp. 766-768, 1989.
9. Shiraishi, K. et al., *Japanese Journal of Applied Physics*, Vol. 28, No. 5, pp. 807-808, 1989.
10. Shiraishi, K. et al., *Japanese Journal of Applied Physics*, Vol. 27, No. 12, pp. 2339-2341, 1988.
11. Nastasi, M. et al., *Applied Physics Letters*, Vol. 53, No. 14, pp. 1326-1328, 1988.
12. Vichery, H. et al., *Physica C*, Vol. 159, pp. 697-706, 1989.

13. Rullier-Albenque, F. et al., *Solid State Communications*, Vol. 66, No. 4, pp. 417-420, 1988.
14. Hofmann, A. et al., *Physica C*, Vol. 153-155, pp. 341-342, 1988.
15. Knoll, G. F., *Radiation Detection and Measurement*, John Wiley and Sons, Inc., 1979.
16. Rudie, N. J., *Principles and Techniques of Radiation Hardening*, Vol. 1 , 3rd Ed., Western Periodicals Co., 1986.
17. Maruyama, X. K. et al., *Nuclear Instruments and Methods in Physics Research*, A272, 237-240, 1988.
18. Hungerford, E.V (TCSUH) *Private Communication*.
19. Reid, C., *Procedures for Electron Beam Emittance and Profile Measurements Using Optical Transition Radiation*, Master's Thesis, Naval Postgraduate School, Monterey, California, December 1990.
20. Evans, R. D., *The Atomic Nucleus*, McGraw-Hill Book Company, 1955.
21. Krane, K. S., *Introductory Nuclear Physics*, John Wiley and Sons, Inc., 1988.
22. Feiner F., Miller, D. G., and Walker, W. F., *Chart of the Nuclides*, 13th ed., General Electric Co., 1984.
23. Serway, R. A., *Superconductivity Supplement for Physics for Scientists and Engineers*, 2nd ed., Saunders College Publishing, 1988.
24. Cava, Robert J., "Superconductors beyond 1-2-3," *Scientific American*, August 1990.
25. Kittel, C., *Introduction to Solid State Physics*, Sixth Edition, John Wiley and Sons, Inc., 1986.

BIBLIOGRAPHY

1. Evans, R. D., *The Atomic Nuclius*, McGraw-Hill Book Company, 1955.
2. Halliday, D. and Resnick, R., *Fundamentals of Physics*, Third Edition, John Wiley and Sons, Inc., 1988.
3. Hazen, R. M., *The Breakthrough--The Race for the Superconductor*, Summit Books, 1988.
4. Knoll, G. F., *Radiation Detection and Measurement*, John Wiley and Sons, Inc., 1987.
5. Krane, K. S., *Introductory Nuclear Physics*, John Wiley and Sons, Inc., 1987.
6. Myers, H. P., *Introductory Solid State Physics*, Taylor and Francis, 1990.

INITIAL DISTRIBUTION LIST

		No. of Copies
1.	Defense Technical Information Center Cameron Station Alexandria, VA 22304-6145	2
2.	Library, Code 52 Naval Postgraduate School Monterey, CA 93943-5002	2
3.	Professor X. K. Maruyama, Code PH/Mx Department of Physics Naval Postgraduate School Monterey, CA 93943-5002	4
4.	Professor Kai Woehler, Code PH/Wh Department of Physics Naval Postgraduate School Monterey, CA 93943-5002	1
5.	LT Sean M. Connors, USN 3110 Teal Lane Bowie, MD 20715	2
6.	Professor F. R. Buskirk, Code PH/Mx Department of Physics Naval Postgraduate School Monterey, CA 93943-5002	1
7.	Don Snyder, Code PH/Mx Department of Physics Naval Postgraduate School Monterey, CA 93943-5002	1

- | | | |
|----|---|---|
| 8. | Harold Rietdyk, Code PH/Mx
Department of Physics
Naval Postgraduate School
Monterey, CA 93943-5002 | 1 |
| 9. | Jeff Bechtold
Texas Center of Superconductivity
University of Houston
Houston, TX 77204-5932 | 1 |